Preprint typeset using LaTeX style emulateapj v. 08/22/09

arXiv:0909.4813v1 [astro-ph.CO] 25 Sep 2009

MAPPING THE SPATIAL DISTRIBUTION OF DUST EXTINCTION IN NGC 959 USING BROADBAND VISIBLE AND MID-IR FILTERS

K. Tamura[1], R. A. Jansen[2,1] and R. A. Windhorst[2,1]

(Accepted for publication in AJ 2009 September 24)

ABSTRACT

We present a method to estimate and map the two-dimensional distribution of dust extinction in the late-type spiral galaxy NGC 959 from the theoretical and observed flux ratio of optical V and mid-IR (MIR) $3.6\,\mu$m images. Our method is applicable to both young and old stellar populations for a range of metallicities, and is not restricted to lines-of-sight toward star-formation (SF) regions. We explore this method using a pixel-based analysis on images of NGC 959 obtained in the V-band at the Vatican Advanced Technology Telescope (VATT) and at $3.6\,\mu$m (L-band) with *Spitzer*/IRAC. We present the original and extinction corrected *GALEX* far-UV (FUV) and near-UV (NUV) images, as well as optical *UBVR* images of NGC 959. While the dust lanes are not clearly evident at *GALEX* resolution, our dust map clearly traces the dust that can be seen silhouetted against the galaxy's disk in the high-resolution *HST* images of NGC 959. The advantages of our method are: (1) it only depends on two relatively common broadband images in the optical V-band and in the MIR at $3.6\,\mu$m (but adding a near-UV band improves its fidelity); and (2) it is able to map the two-dimensional spatial distribution of dust within a galaxy. This powerful tool could be used to measure the detailed distribution of dust extinction within higher redshift galaxies to be observed with, e.g., the *HST*/WFC3 (optical–near-IR) and *JWST* (mid-IR), and to distinguish properties of dust within galaxy bulges, spiral arms, and inter-arm regions.

Subject headings: dust, extinction — galaxies: individual (NGC 959) — galaxies: spiral — galaxies: structure

1. INTRODUCTION

Dust extinction is a longstanding problem when studying stellar populations within our Galaxy and in extragalactic objects (e.g., Trumpler 1930; Mathis et al. 1977; Viallefond et al. 1982; Caplan & Deharveng 1985; Roussel et al. 2005; Driver et al. 2008). Variations in the amount and the spatial distribution of interstellar dust have different effects on the light from background stellar populations (e.g., Elmegreen 1980; Walterbos & Kennicutt 1988; Waller et al. 1992; Witt et al. 1992; Calzetti et al. 1994; Deo et al. 2006). Measuring and correcting for dust extinction in individual galaxies is important to understand the true nature of their stellar populations, especially when one aims to study small-scale structures such as H II regions of spiral galaxies, which tend to be particularly dusty (e.g., Petersen & Gammelgaard 1997; Scoville et al. 2001; Calzetti et al. 2005).

Many different methods are used to estimate dust extinction within target galaxies. Some commonly used methods involve: (1) the ratios of Hydrogen recombination-line fluxes for H II regions, e.g., Hα/Hβ (e.g., Caplan & Deharveng 1985, 1986; Maíz-Apellániz et al. 2004; Roussel et al. 2005; Relaño et al. 2006) or of Hα/Paα (e.g., Petersen & Gammelgaard 1997; Scoville et al. 2001; Calzetti et al. 2005, 2007); (2) the ratio of the FIR and UV fluxes (e.g., Buat & Xu 1996; Calzetti et al. 2000, 2005, 2007; Charlot & Fall 2000; Witt & Gordon 2000; Bell et al. 2002a; Boselli et al. 2003; Panuzzo et al. 2003; Boissier et al. 2004); (3) the UV spectral slope (e.g., Calzetti et al. 1994; Meurer et al. 1999; Bell 2002b); and (4) the CO column density from (sub-)millimeter observations of, e.g., ^{12}CO($J=1$–0) line and $J=1$–0 and $J=2$–1 transitions of ^{13}CO and C^{18}O (Encrenaz et al. 1975; Dickman 1978; Frerking et al. 1982; Harjunpää & Mattila 1996; Hayakawa et al. 1999, 2001; Harjunpää et al. 2004).

Even though all these methods measure dust extinction in some way, each has its limitations. The Balmer decrement, Hα/Hβ, and the Hα/Paα flux ratios are generally limited to lines-of-sight toward H II regions. These H II regions can be distributed all over a galaxy, but cover only a small fraction of an entire galaxy disk (e.g., Scoville et al. 2001). Accurate measurements of the underlying Balmer absorptions from moderate-resolution spectra are also required (Petersen & Gammelgaard 1997; Boissier et al. 2004). The FIR/UV flux ratio can be used throughout a galaxy, although the spatial resolution in the FIR is generally poor: about $\sim 20''$ for the Midcourse Space Experiment (MSX) at 4.2–26$\,\mu$m (Price et al. 2002), $\sim 40''$ for *Spitzer*/MIPS at $160\,\mu$m (Rieke et al. 2004), and even larger ($\sim 100''$) for IRAS at $100\,\mu$m (Xu & Helou 1996; Boissier et al. 2004). This becomes a significant limitation in studying small-scale structural features, and limits access to only the very nearest galaxies. Unlike the FIR images, the UV images can have much higher resolution (FWHM$\lesssim 0.''1$) with the *HST* WFPC2 and ACS (Trauger et al. 1994; Sirianni et al. 2005), or FWHM$\lesssim 4$–$6''$ for *GALEX* (Morrissey et al. 2005). A major complication of methods involving UV

Electronic address: ktamura@asu.edu
[1] Department of Physics, Arizona State University, Tempe, AZ 85287-1504, USA; `ktamura@asu.edu`
[2] School of Earth and Space Exploration, Arizona State University, Tempe, AZ 85287-1404, USA; `rolf.jansen@asu.edu`, `rogier.windhorst@asu.edu`

filters (FIR/UV flux ratio and UV spectral slope) is that the UV emission is significantly affected not only by dust, but also by the age and metallicity of stellar populations. Finally, sub-millimeter and millimeter observations are used to measure the column density of CO molecules directly, and hence — under certain assumptions — that of molecular hydrogen, H_2. The CO (and hydrogen) column density is converted to extinction using the correlation found between CO and dust-extinction in nearby galaxies (e.g., Dickman 1978; Bachiller & Cernicharo 1986; Komugi et al. 2005). The typical resolution at millimeter wavelengths is poor (FWHM $\simeq 20''$–$2'\!.6$; Encrenaz et al. 1975; Dickman 1978; Frerking et al. 1982; Harjunpää & Mattila 1996; Hayakawa et al. 1999, 2001; Harjunpää et al. 2004), although ALMA (Brown et al. 2004) will soon greatly improve on this. Studies such as that of Boissier et al. (2007) also show that the relationship between the dust column density and the amount of extinction is complicated, and that further study is necessary to derive the relationship between the two values.

Without using these methods, Regan (2000) investigated dust extinction using the more commonly used ground-based optical *BVRI* and near-IR (NIR) *JHK* filters to obtain various color maps. The advantage of using optical–NIR filters is that the extinction measurement is independent of the dust temperature (Regan 2000), and that the images can have much higher spatial resolution at these wavelengths (e.g., Regan & Mulchaey 1999). Combining theoretical models and color maps from optical–NIR images, the spatial dust distribution can then be derived. Fig. 7 of Regan (2000) shows that this method can reconstruct extinction-free galaxy images. However, as Regan (2000) points out, there are several issues with this particular method. The first is that all of the bandpasses involved are affected by the dust to some degree: no single optical–NIR filter directly maps either stellar or dust morphology by itself. The second issue is that, while the intrinsic colors of the underlying stellar populations are well known for the older stellar populations, the colors of younger stellar populations in star-formation (SF) regions vary, depending on their environment and specific properties. Since Regan (2000) treated all stellar populations as old stellar populations, the extinction measurements for stellar populations in SF-regions are less accurate and should be treated with care, as their paper points out.

In this paper, we will map the two-dimensional spatial distribution of dust extinction in NGC 959, using images from commonly used optical–MIR filters. Many images observed with optical–MIR filters from both ground and space are now readily available for large samples of galaxies though publicly available archives. We will also treat the younger stellar populations separately from older stellar populations to measure dust extinction in SF-regions. We initially combine data spanning the *GALEX* FUV and NUV, the ground-based optical *UBVR* filters, the 2MASS NIR JHK_s filters, and the *Spitzer*/IRAC 3.6, 4.5, 5.8, and 8.0 μm (MIR) filters. The IRAC 3.6 and 4.5 μm filters are not nearly as affected by dust extinction as the NIR filters, and therefore are commonly used to trace the distribution of stellar populations (e.g., Willner et al. 2004). We use the library of spectral energy distributions (SEDs) by Anders & Fritze-von Alvensleben (2003, hereafter AF03), to study possible combinations of filters and colors in the analysis of dust extinction. Using a pixel-based analysis (e.g., Bothun 1986; Abraham et al. 1999; Eskridge et al. 2003; Lanyon-Foster et al. 2007; Welikala et al. 2008) on NGC 959, we will demonstrate that our method can reveal a two-dimensional distribution of dust extinction.

This paper is organized as follows. In §2, we present our method to estimate dust extinction using the SED models. In §3 and §4, we test and apply this method to all available images for the nearby late-type spiral galaxy NGC 959. We give a discussion of our results in §5, and present our conclusions in §6.

2. MODELS AND CONCEPT

Before we analyze any observed images, we first evaluate theoretical SED models for single stellar populations (SSPs) at different ages and metallicities. In this section, we describe the SED library that we used in our study, and then select the optimal filters for the subsequent SED analysis. Once the filters are selected, we describe how to estimate the dust extinction, using the theoretical SEDs and observed images, through flux ratios of an optimal set of filters.

2.1. *Simple Stellar Population Models*

Among published SSP SED libraries (e.g., AF03; Bruzual & Charlot 2003; Maraston 2005), we elected to use the SED library by AF03. While other SED libraries do not contain information about emission lines, this library includes both spectral and gaseous emission for young stellar populations. AF03 has created multiple sets of SED libraries[3] of SSPs, using the Padova (Bertelli et al. 1994) and Geneva (Lejeune & Schaerer 2001) isochrone models with Scalo (1986), Salpeter (1955), and Kroupa (2002) Initial Mass Functions (IMFs). These SED libraries contain models for metallicities of Z = 0.0004, 0.004, 0.008, 0.02 (Solar), and 0.04. Both isochrone models include the thermally pulsing asymptotic giant branch (TP-AGB) phase and model atmosphere spectra from Lejeune et al. (1997). The main difference between the two libraries with different isochrone models is the time resolution, Δt. While the library with the Padova isochrones have an age coverage from 4 Myr to 14 Gyr with $\Delta t = 4$ Myr up to an age of 2.35 Gyr, and $\Delta t = 20$ Myr for older ages, the library with the Geneva isochrones have variable time steps. Among the available models, we will focus on the ones computed with Padova isochrones and the Scalo IMF — adopting an upper mass limit of $\sim 50\,M_\odot$ for super-solar metallicity, and $\sim 70\,M_\odot$ for all other metallicities. We refer the reader to AF03 and references therein for a detailed description of this library. The SEDs of SSPs change rapidly at all wavelengths, but especially so in the UV for ages younger than ~ 100 Myr (see Fig. 1). Once a stellar population reaches the age of ~ 500 Myr, the rate of change in SED diminishes with increasing age. As a

---

[3] Since the publication of Anders & Fritze-von Alvensleben (2003), there have been several updates and additions to their models, resulting in slightly different combinations of IMFs and metallicities from the original description. We used the version dated 28 October, 2007.
`http://www.galev.org/`

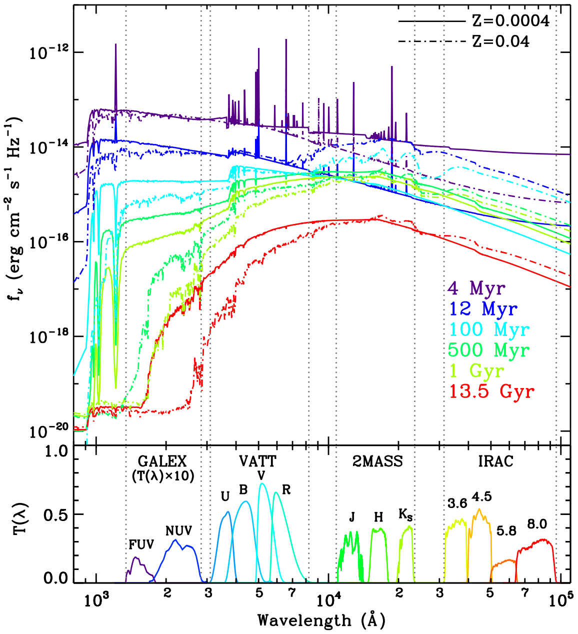

Fig. 1.— *Top panel*: Theoretical SEDs from the library of Anders & Fritze-von Alvensleben (2003). Among the different sets of isochrones and IMFs, SEDs for Padova isochrones assume a Scalo IMF with metallicity of 0.0004 (solid curves) and 0.04 (dash-dot curves) at 6 different ages as indicated. The age-metallicity degeneracy is clearly visible for wavelengths shortward of 4000 Å. On the other hand, SEDs at $\lambda \gtrsim 6000$ Å are less affected by metallicity, except for extremely young ($t \lesssim 100$ Myr) stellar populations. *Bottom panel*: Total throughput curves, T(λ), for different telescope-filter combinations. Throughput for the *GALEX* filters are scaled up by a factor of 10 for better visibility. Vertical dotted lines indicate the wavelength coverage for each telescope-filter combination.

practical subset for our analysis, we consider 10 different ages ($t = 4$, 8, 12, 52, 100, 500 Myr, 1, 5, 10, and 13.5 Gyr) for each metallicity, resulting in a model grid of 50 different SEDs. In the main panel of Fig. 1, we plot the SEDs for six ages and two metallicities that span the full range of our adopted model grid.

2.2. *Optimal Filter Selection*

The bottom panel of Fig. 1 shows the total throughput curves, $T(\lambda)$, for various FUV–MIR filters considered in this study, as well as in the subsequent multiwavelength studies on NGC 959 and on a sample of 45 galaxies (Tamura et al. 2009b,c, in preparation). Total throughput curves for the *GALEX* filters — published in Morrissey et al. (2005) and on the *GALEX* web page[4] — are multiplied by a factor of 10 for better visibility. The throughput curves for the VATT filters are the total responses of the filters, CCD, and telescope[5]. The throughput curves for the 2MASS JHK_s filters are the total responses of the filters, CCD, telescope, and atmosphere[6]. Finally, for the *Spitzer*/IRAC filters, the total throughput curves are calculated using all components of the *Spitzer* instrument[7]. The vertical dotted lines in Fig. 1 indicate the wavelength ranges covered by different telescopes and instruments.

The largest change in SEDs with the increase in age is the reduction of flux for wavelengths shortward of 4000 Å. Especially the UV flux — as measured by, e.g., the *GALEX* FUV and NUV filters — decreases by up to ∼6 dex relative to the maximum flux level, as an SSP ages from 4 Myr to 13.5 Gyr. SEDs are also significantly affected by metallicity. For SSPs older than 100 Myr, the metallicity mainly affects the wavelengths $\lesssim 4000$ Å, where the flux decreases by up to ∼2 dex from $Z = 0.0004$ to $Z = 0.04$. Since our primary goal is to measure dust extinction and to map its spatial distribution, filters covering wavelengths shorter than 4000 Å should be avoided to minimize effects from the age-dust-metallicity degeneracy.

According to AF03, the model SEDs become uncertain longward of $\sim 5\,\mu$m. Also, the observed stellar continuum at MIR wavelengths redward of $\sim 5\,\mu$m is contaminated by emission from polycyclic aromatic hydrocarbons (PAHs; Leger & Puget 1984) and silicates (Willner et al. 2004). We thus exclude *Spitzer*/IRAC 4.5, 5.8, and 8.0 μm filters. On the other hand, the effects from dust extinction and emission by PAHs and silicates reach a minimum near 3.5 μm (*L*-band; e.g., Fazio et al. 2004; Willner et al. 2004). The IRAC 3.6 μm filter therefore provides the most reliable stellar population tracer (see, e.g., Kennicutt et al. 2003; Helou et al. 2004).

From the filters with $0.4 \lesssim \lambda \lesssim 3.5\,\mu$m — optical VR and NIR JHK_s in our study — we need to select (at least) one more filter to trace dust extinction. Since dust extinction is much smaller in the NIR than in the optical V- and R-bands (e.g., van Houten 1961; Cardelli et al. 1989; Calzetti et al. 1994; Gordon et al. 2003), NIR filters are not optimal for this purpose. Another reason to avoid ground-based NIR observations is absorption due to atmospheric water vapor. The amount and uncertainty due to this absorption depend on atmospheric conditions, as well as the location of the observations (e.g., Nitschelm 1988; Cohen et al. 2003). Dust extinction is stronger in the V-band (e.g., Calzetti et al. 1994; Gordon et al. 2003), while the metallicity effects are slightly weaker (see Fig. 1). We therefore choose the V and 3.6 μm filters to globally trace the dust extinction. In the following section, we will explore the theoretical V-to-3.6 μm flux ratio in detail, and explain how we can use this ratio to estimate dust extinction. For other studies, in general, it should be noted that filters like SDSS g, *HST* F555W, F550M, and F606W would be adequate substitutes for V-band after calibration of the theoretical flux ratios.

2.3. *Theoretical V-to-3.6 μm Flux Ratio Map*

---

[4] Goddard Space Flight Center, the *GALEX* Post Launch Response Curve Data:
`http://galexgi.gsfc.nasa.gov/docs/galex/Documents/PostLaunchResponseCurveData.html`

[5] Instrumentation for VATT:
`http://vaticanobservatory.org/vattinst.html`
The response curve used in this paper is for the VATT 2k CCD.

[6] 2MASS All-Sky Data Release Explanatory Supplement Facilities and Operations:
`http://www.ipac.caltech.edu/2mass/releases/allsky/doc/sec3_1b1.html`

[7] Spitzer Science Center: IRAC: Spectral Response:
`http://ssc.spitzer.caltech.edu/irac/spectral_response.html`

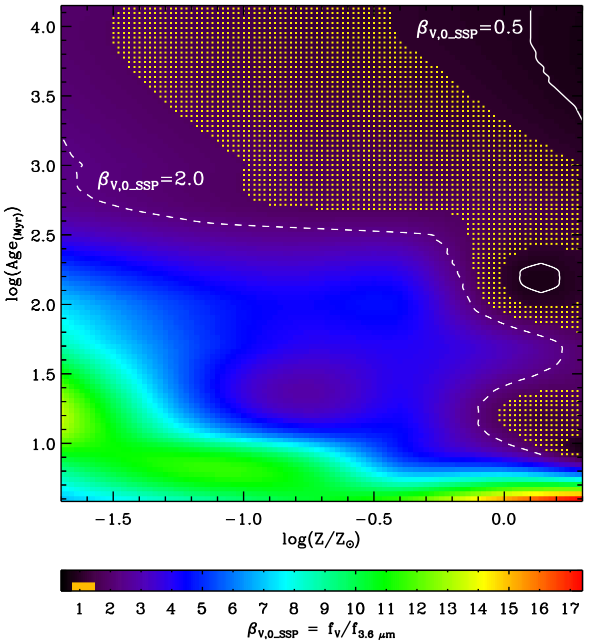

FIG. 2.— Map of the theoretical V-to-3.6 μm flux ratio, β_V, calculated from an SSP library of Anders & Fritze-von Alvensleben (2003) for varying age and metallicity. Contours are plotted at $\beta_V = 0.5$ (solid curves) and 2.0 (dashed curve). The orange stippled region (and the orange band in the color bar) indicates the regions in the metallicity-age space where the flux ratio is $0.75 \leq \beta_V \leq 1.50$. While β_V varies rapidly for young — $t \lesssim 500$ Myr or $\log(t_{\rm Myr}) \lesssim 2.7$ — stellar populations, it is relatively stable and insensitive to age and metallicity for older stellar populations.

Given the SEDs from the AF03 library and the throughput curves of the optical V and IRAC 3.6 μm filters (see Fig. 1), we explore the range in the theoretical flux ratio, $\beta_V = f_V/f_{3.6\,\mu{\rm m}}$, as a function of age and metallicity. The resulting flux ratio map in age-metallicity space is shown in Fig. 2. From the input of 50 SEDs described above, both age and metallicity are resampled logarithmically using 100 steps with Spline interpolation to map the variation in β_V values over the full parameter ranges. The minimum ratio, $\beta_{V,{\rm min}} = 0.39$, occurs for the most metal-rich ($Z = 0.04 = 2Z_\odot$) and oldest ($t = 13.5$ Gyr) SSP, while the maximum ratio, $\beta_{V,{\rm max}} = 17.4$, is found for the most metal-rich and the youngest ($t = 4$ Myr) SSP. Contours for $\beta_V = 0.5$ (white solid curves) and 2.0 (white dashed curve) are drawn in Fig. 2. A band of orange dots — also included as an orange band in the color bar — indicates the region where the V-to-3.6 μm flux ratio spans the range $0.75 \leq \beta_V \leq 1.50$.

For stellar populations older than 500 Myr, or $\log(t_{\rm Myr}) \gtrsim 2.70$, the theoretical flux ratio changes little as a function of age and metallicity. Fig. 2 shows that β_V ranges mostly between ~ 0.5 and ~ 2.0. On the other hand, for stellar populations younger than 500 Myr, β_V changes more dramatically, depending on their age and metallicity. Especially for SSPs with super-solar metallicity, β_V changes from ~ 17 (red) for the youngest SSPs to $\lesssim 0.5$ (dark purple/black) in a matter of only a few 100 Myr. For the young SSPs with sub-solar metallicities, the value of β_V is more stable, but still changes much more rapidly than for SSPs older than 500 Myr. Among these young sub-solar metallicity SSPs, Fig. 2 shows two distinctive ranges of β_V values: (1) a band color-coded in green ($9 \lesssim \beta_V \lesssim 13$) for SSPs younger than 10–100 Myr; and (2) a band coded in blue ($4 \lesssim \beta_V \lesssim 7$) for SSPs up to ~ 500 Myr.

The distribution of β_V values in Fig. 2 confirms the assumption of, e.g., Regan (2000): that old stellar populations have relatively constant color, while young stellar populations change their colors more rapidly depending on their properties and environments. An important corollary of the former is that a mixture of SSPs with ages larger than 500 Myr will have a β_V value that is very similar to that of a single SSP at those ages. Our analysis of the theoretical V-to-3.6 μm flux ratios furthermore shows that — at least for young stellar populations with sub-solar metallicities — the theoretical flux ratio can be approximated as being constant for stellar populations in either of the two age ranges ($t \lesssim$ 10–100 Myr or 10–100 $\lesssim t \lesssim 500$ Myr) described above. In the following section, we will derive a method for using these theoretical and observed V-to-3.6 μm flux ratios to estimate the amount and spatial distribution of dust extinction in the V-band.

2.4. *Estimating the V-band Dust Extinction, A_V*

In the previous section, we showed that the theoretical V-to-3.6 μm flux ratio, β_V, is well-behaved, particularly for sub-solar metallicities. To estimate the dust extinction for an observed stellar population, we first have to determine its approximate age and metallicity. The appearance of horizontal bands of different β_V values in Fig. 2 indicates that an age determination is more important than the determination of metallicity. Based on the β_V values and corresponding age range for different metallicities as described above, the accuracy required in determining age is ~ 0.5 dex for extremely metal poor stellar populations, and ~ 1 dex for sub-solar to solar metallicity and older ($t \gtrsim 500$ Myr) stellar populations. For stellar populations with super-solar metallicities, the accuracy required is also $\sim$0.5–1 dex for most ages, unless they are extremely young ($t \lesssim 10$ Myr). The use of color-magnitude diagrams (CMDs) and color-color diagrams, therefore, should suffice to estimate the age of a stellar population and select a theoretical β_V value from Fig. 2. By comparing the theoretical and observed flux ratios, we can infer the amount of flux missing in the V-band observation due to dust. The missing flux is a very robust property of the dust distribution, independent of the geometry and fine structure of obscuration. The amound of extinction by dust along the line-of-sight that this stellar pouplation suffers can then be estimated from this missing V-band flux.

The dust extinction, A_V, is defined as

$$A_V = (m_V - m_{V,0})\,, \tag{1}$$

where m_V and $m_{V,0}$ denote the observed and intrinsic (extinction-free) V-band magnitudes, respectively. Even though the extinction-free magnitude is not known for an observed stellar population, we can use the selected β_V value and observed 3.6 μm flux to estimate the predicted $m_{V,0}$. Since we assume that the observed 3.6 μm flux is unaffected by dust extinction (e.g., Fazio et al. 2004; Willner et al. 2004), we can estimate the extinction-free

V-band flux by multiplying the selected theoretical β_V value with the observed 3.6 μm flux:

$$f_{V,0} = \beta_V \times f_{3.6\,\mu\mathrm{m}}\,. \tag{2}$$

Therefore, equation (1) can be rewritten as

$$A_V = m_V - [-2.5\log(\beta_V \times f_{3.6\,\mu\mathrm{m}}) - V_{\mathrm{zp}}]\,, \tag{3}$$

where V_{zp} is the zero-point magnitude for the V-band. Compared to popular methods such as the UV spectral slopes (e.g., Bell 2002b; Kong et al. 2004) and the FIR-to-UV flux ratio (e.g., Dale et al. 2001; Buat et al. 2005), this method is much simpler.

Even though our prescription is simple, there remain many possible sources of error. In addition to the usual uncertainties due to observational measurements, there are several sources of uncertainty in the selected theoretical β_V value. Only when the age and metallicity are known for a resolved stellar population can we determine β_V for this stellar population with minimal error. For unresolved stellar populations, determining the age and metallicity becomes much harder as a result of light-blending from intermixed and superposed stellar populations. As we have shown above, the metallicity dependency is not as strong as the age dependence in determining the likely β_V value. We therefore are still able to estimate the β_V value, if an approximate age of the stellar populations can be determined. Even though stellar population composites span a range in age, their luminosity tends to be dominated by their younger components at most wavelengths (see Fig. 1). From the distribution of β_V values in Fig. 2, we find a typical uncertainty in the determination of β_V for a stellar population of a factor of ~ 1.4 (e.g., assuming a theoretical $\beta_V = 1.1$, an old stellar population may actually show a range of $0.75 \lesssim \beta_V \lesssim 1.5$). This corresponds to an error in dust extinction, σ_{A_V}, of up to $\sim \pm 0.37$ mag, or mag arcsec^{-2} in the case of surface brightness. If this stellar population is either extremely metal-poor or metal-rich, the uncertainty is a factor of ~ 2, or $\sigma_{A_V} \simeq \pm 0.75$ mag. On the other hand, if an extremely young (old) stellar population is treated as an old (extremely young) stellar population, the error in the estimated theoretical β_V value will become a factor of ~ 5 or larger. This corresponds to a significant error in estimating the dust extinction, with $\sigma_{A_V} \gtrsim \pm 1.75$ mag. Since the extremely young and old stellar populations usually have distinct characteristics in the CMDs and color-color diagrams, it is highly unlikely that one would mistake a young stellar population for an old one. In §3.3 below, we will use U-band observations to robustly separate pixels dominated by the light of younger and older stellar populations.

3. DATA ANALYSIS

In this section, we apply the above method to the observational data. Before applying it to a large sample of galaxies, we assess its reliability in this paper for one galaxy: NGC 959. In future papers (Tamura et al. 2009b,c, in preparation), we will reconstruct and analyze the extinction-corrected images of NGC 959 and a sample of 45 galaxies, spanning a wide range of elliptical–spiral galaxies, with *GALEX* FUV and NUV, optical *UBVR*, and *Spitzer*/IRAC images using the present method. Unless indicated otherwise, the color composite images and the pixel coordinate maps shown in the following sections are oriented such that North is up and East is to the left. The magnitudes and colors used in this analysis are on the AB-magnitude system (Oke 1974; Oke & Gunn 1983).

3.1. *Data Sets*

The galaxy we will use for our proof of concept, NGC 959, is a nearby late-type spiral galaxy classified as Sdm in the Third Reference Catalog of Bright Galaxies (RC3; de Vaucouleurs et al. 1991), at a distance of 9.9 ± 0.7 Mpc[8] (Mould et al. 2000), with an inclination of 50° (Esipov et al. 1991). It has been observed from UV (*GALEX* FUV) through MIR (*Spitzer*/IRAC 8.0 μm) wavelengths. Optical *UBVR* images, observed with the Vatican Advanced Technology Telescope (VATT), were taken from Taylor et al. (2005). The pipeline-processed *Spitzer*/IRAC images were retrieved from the *Spitzer* Archive[9] via Leopard. The *GALEX* FUV and NUV images were obtained from the Multi-Mission Archive at Space Telescope Institute[10] (MAST).

In this study, we use a pixel-based analysis, first introduced by Bothun (1986) in the form of pixel Color-Magnitude Diagrams (pCMDs). This has recently become a popular technique to study stellar populations in nearby galaxies (e.g., Abraham et al. 1999; Eskridge et al. 2003; Lanyon-Foster et al. 2007; Welikala et al. 2008). This technique is performed in the same way as regular aperture photometry, but simply with an individual pixel as a source of flux. The advantage of using a pixel-based analysis is that this technique allows a two-dimensional analysis throughout a galaxy, or any part of a galaxy, without any object overlap or gaps as would be created in regular aperture photometry (see figures by, e.g., Scoville et al. 2001; Calzetti et al. 2005, 2007).

To perform this pixel-based analysis on images from different telescopes and instruments, we first have to resample the pixel-scales and convolve all the images to a matching resolution. IDL[11] and IRAF[12] routines were used to match the pixel-scales and point spread functions (PSFs) of all images to the $1''\!.5$ pixel^{-1} and $\sim 5''\!.3$ FWHM of the *GALEX* NUV image, because these have the coarsest pixel-scale and PSF among the filters considered for further panchromatic (FUV–MIR) studies (see Fig. 1 and Tamura et al. 2009b,c, in preparation). At the distance of NGC 959 ($\mathrm{D} = 9.9 \pm 0.7$ Mpc), each $1''\!.5$ pixel spans 72 pc. As a result, the light from different stellar populations is mixed together within a single pixel, and the observed flux ratios cannot be compared directly to the SSP-derived β_V values in Fig. 2. While the pixels with most of the light coming from older stellar populations are not affected as much, the pixels with light from younger stellar populations will be affected significantly. Even though the light is smoothed over a much larger area than the area covered by a single pixel, the peak of the light distribution stays at the same pixel coordinate as before the smoothing. In the following, we therefore statistically analyze the observed images to estimate the intrinsic, dust-free flux ratios for both younger and older stellar populations, instead of a direct comparison to SSP models in the previous section. We will only use pixels with signal-to-noise ratio of $\mathrm{S/N} \geq \mathrm{S/N}_{\mathrm{min}} = 3.0$ in all FUV–MIR filters used.

---

[8] This value is based on its recession velocity including the influence of the Virgo cluster, the Great Attractor, and the Shapley supercluster, and taken from the NASA/IPAC Extragalactic Database (NED) as of September 24, 2008

[9] SSC: Data Archives/Analysis: `http://ssc.spitzer.caltech.edu/archanaly/`

[10] Galaxy Evolution Explorer, GR4/GR5 Data Release: `http://galex.stsci.edu/GR4`

[11] IDL is distributed by ITT Visual Information Solutions (Research System Inc.), Boulder, Colorado: `http://rsinc.com/idl/`

[12] IRAF is distributed by National Optical Astronomy Observatory (NOAO), which is operated by the Association of Universities for Research in Astronomy, Inc., under cooperative agreement with the National Science Foundation (NSF): `http://iraf.net`

3.2. *Assumptions about the Dust Distribution*

The dust is not uniformly distributed across an entire galaxy. Instead, it is distributed in complicated patterns of wisps, lanes, and bands of thin and filamentary structures, as well as in small clumps (e.g., Waller et al. 1992; Deo et al. 2006). Using stellar radiative transfer models, Elmegreen (1980) and Witt et al. (1992) showed that depending on different spatial distributions of the dust, e.g., a cloud or a slab, the effect of dust extinction — including both absorption and scattering — varies along different lines-of-sight. Walterbos & Kennicutt (1988) estimated the variations in extinction values calculated from the "symmetry argument" (e.g., Lindblad 1941; Elvius 1956). Calzetti et al. (1994) compared models of five different dust distributions to the observational data: (1) a uniform dust screen; (2) a clumpy dust screen; (3) a uniform scattering slab; (4) a clumpy scattering slab; and (5) an internal dust model (see their Fig. 8). The importance of these models is that the resulting extinction is different for each model although the amount of dust is same. Even though Calzetti et al. (1994) could not find satisfactory agreement between the observed data and these models using Large Magellanic Cloud (LMC) or Milky Way (MW) dust-extinction curves, models 2 and 4 with clumpy dust distributions show in general a better fit to the data than the other models. We will assume that the dust affecting the observed light is distributed in wisps and clumps, and is mostly in front of the observed stellar populations — with a much larger effect of absorption than light scattering (Byun 1992) — following the observations of, e.g., Waller et al. (1992) and Deo et al. (2006). The true distribution of the dust would be more complex, but representable by a combination of different types of simple geometrical distributions, with the dust distributed not only in front, but also intermixed with stellar populations. Dust located mostly behind the stars would not be detected at the wavelengths considered here. Decoding the distribution of dust in different geometries is beyond the scope of the present paper, and hence deferred to a subsequent analysis (Tamura et al. 2009c, in preparation), where we will have a larger sample of galaxy types and inclinations.

Another important issue is the filling factor of dust within a pixel. While each pixel subtends $1\farcs5$, the dust features can span either a larger or smaller area. Given a single average value of the dust extinction in each pixel, there are two extreme possibilities for the dust distribution within that pixel: (1) an extended distribution of a relatively thin layer of dust; and (2) small high-density clumps of dust covering only a fraction of the area in that pixel. Since the light observed in a single pixel is a mixture of light from different stellar populations, the effect that we observe is a weighted average of the light from those stellar populations. For the former type of dust distribution, the dust is affecting the light of all stellar populations contributing to a single pixel equally. For the latter case, the dust is only affecting a small fraction of the total light in that pixel. While the light from stellar populations behind a dust clump is reduced, the light from unextincted stellar populations is observed at its full strength, reducing the average effect of dust extinction within a pixel. If the intrinsic V-band flux is estimated from the observed NIR-flux — which is still affected by dust extinction to some degree — this partial coverage of any dust extinction might cause a large uncertainty. Our method, on the other hand, estimates the intrinsic V-band flux from the observed MIR ($3.6\,\mu$m) flux, which is usually considered as extinction free (e.g., Fazio et al. 2004; Willner et al. 2004). The observed $3.6\,\mu$m flux is therefore the *total* light from all stellar populations along the line-of-sight, ranging from the front to the far side of a galaxy. Since the intrinsic V-band flux is estimated based on this $3.6\,\mu$m flux, our method estimates the *total* amount of missing V-band flux. Hence, even though the "exact" effect of dust extinction depends on the true dust geometry, the *total* missing V-band flux and the corresponding dust extinction should not be affected by the dust geometry, unless the extinction in individual knots or filaments is $\gg 1.0$ mag, thereby also affecting the observed MIR flux, and preferentially affecting only young and highly concentrated (on scales $\ll 72$ pc) stellar populations. In retrospect, this does not appear to be the case (see e.g., Fig. 11), although one has to be careful that this does not become a circular argument.

3.3. *Separating Younger and Older Stellar Populations*

Even though the effect of light-blending is significant in NGC 959, some pixels are still dominated by the light from younger stellar populations. Therefore, the first step in our data analysis is to separate these pixels from pixels whose light mostly comes from older stellar populations. Fig. 3 shows theoretical tracks of μ_V vs. $(U{-}3.6\,\mu\mathrm{m})$ using 52 Myr and 10 Gyr SSP SED models with a metallicity of $\mathrm{Z} = 0.008$. These metallicity and ages are selected because: (1) $\mathrm{Z} = 0.008$ is the central metallicity among five metallicities available for the SED library by AF03; (2) $t = 10$ Gyr represents an old stellar population; and (3) $t = 52$ Myr represents a young, but not an extremely young ($t \lesssim 10$ Myr) stellar population (see Fig. 2). Since the U-band light is sensitive to younger stellar populations and $3.6\,\mu$m light traces older stellar populations, the $(U{-}3.6\,\mu\mathrm{m})$ color indicates the luminosity-weighted average age of stellar populations within a given pixel. The solid curve shows a track of the surface brightness and color as the fraction of light from the young stellar population increases. The fraction indicated in the figure is the mass fraction of stellar populations, i.e., "100%" indicates that the mass ratio between young and old stellar populations is one-to-one. A reddening vector corresponding to a visual extinction of $A_V = 1.0$ mag arcsec^{-2} is drawn in the

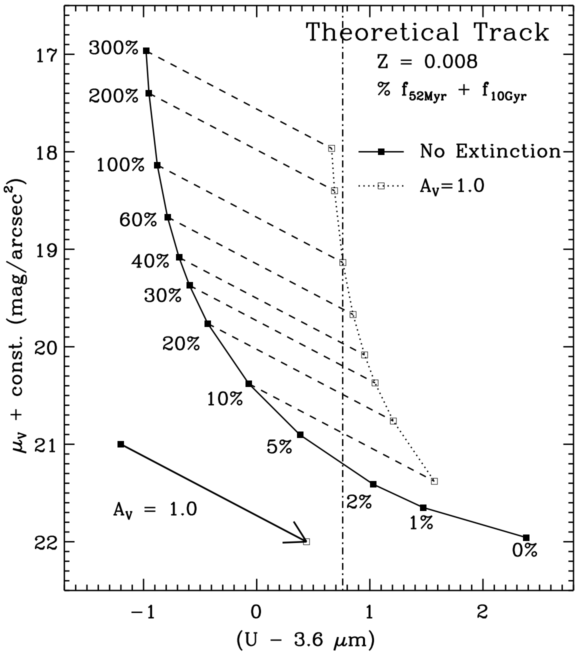

FIG. 3.— The theoretical μ_V vs. $(U{-}3.6\,\mu\mathrm{m})$ color-magnitude diagram. The solid curve is the theoretical track produced by adding different fractions of a young (52 Myr) SSP SED to an old (10 Gyr) SSP SED: the "100%" indicates a mass-ratio between young and old SSPs of 1, and "200%" means the mass-ratio is two-to-one. The effect of an average visual extinction of 1.0 mag arcsec^{-2} is shown as a reddening vector in the lower left, and by dashed lines for selected data-points. The dotted curve traces a theoretical track for the color and surface brightness if the entire pixel (with a filling factor of 100%) is affected by this reddening. The vertical dot-dashed line at $(U{-}3.6\,\mu\mathrm{m}) = 0.76$ mag represents the color where the mass-weighted SEDs of young and old SSPs are contributing equally, and are both affected by a dust extinction of $A_V = 1.0$ mag arcsec^{-2}.

lower left of Fig. 3, and is applied to selected data-points. Even though this is an extreme case, Fig. 3 shows that, once the young stellar population dominates, the color of mixed stellar populations tend to an asymptotic value of $(U{-}3.6\,\mu\mathrm{m}) \simeq -1.0$ mag. In a real situation, younger stellar populations are known to associate with a larger amount of dust (e.g. van Houten 1961; Knapen et al. 1991; Regan et al. 2004; Barmby et al. 2006), and the observed color will therefore most likely shift away from the no-extinction track to redder colors.

Fig. 4a shows a pCMD of μ_V vs. $(U{-}3.6\,\mu\mathrm{m})$ of the observed images at *GALEX* resolution. The photometric uncertainties plotted along the right side of the figure are calculated using data-points within a horizontal slice of $\mu_V \pm 0.1$ mag arcsec^{-2} at each point. A reddening vector corresponding to $A_V = 0.5$ mag arcsec^{-2} and assuming the LMC extinction curve is drawn at the lower left. The stellar populations in NGC 959 are unresolved due to a combination of its distance, the coarse pixel-scale, and a large PSF. As a result, Fig. 4a does not show clear separations among different stellar populations, as are seen for partially resolved stellar populations (e.g., Eskridge et al. 2003). Nevertheless, some branches and features in this pCMD are still recognizable. For simplicity, in the following sections, we will refer to *pixels in which the flux is dominated by light from younger stellar populations* as "younger pixels", and *pixels dominated by older stellar populations* as "older pixels". Visual inspection of Fig. 4a (in particular, different slopes for groups of branching pixels on left and right sides and groups of pixels forming a "shoulder-like" distributions at $\mu_V \simeq 21$ mag arcsec^{-2} in the pCMD) suggests an empirical division between the "younger" and "older" pixels at $(U{-}3.6\,\mu\mathrm{m}) = 0.72$ mag — close to the color indicated by a dash-dotted line at $(U{-}3.6\,\mu\mathrm{m}) = 0.76$ mag in Fig. 3, where young stellar populations start dominating the mass-fraction of a mixed stellar population within a resolution element and suffering a total extinction of $A_V = 1.0$ mag arcsec^{-2}.

Before we proceed, we first perform several visual checks to ensure this separation of younger and older pixels is indeed acceptable. At colors bluer than $(U{-}3.6\,\mu\mathrm{m}) = 0.72$ mag, groups of pixels — or "branch-like features" — seem to have similar slopes as the reddening vector, suggesting that they represent young stellar populations affected by dust. This agrees with the notion (e.g., van Houten 1961; Knapen et al. 1991; Regan et al. 2004; Barmby et al. 2006) that dust is strongly associated with active and recent SF-regions. On the redder side of the pCMD, the brighter pixels ($\mu_V \lesssim 21.9$ mag arcsec^{-2}) form a distribution with a positive slope (i.e., perpendicular to the reddening vector), indicating that a mechanism other than dust extinction might be affecting the fluxes in these pixels. Since the younger stellar populations tend to be much brighter than the older stellar populations (see Fig. 1), for the lower surface brightness (μ_V) pixels, the fraction of light from younger stellar populations as well as its corresponding dust extinction would be smaller. The theoretical tracks in Fig. 3 suggest this would result in a pile-up of points along a fairly vertical line, e.g., the dash-dotted line at $(\mathrm{FUV} - 3.6\,\mu\mathrm{m}) = 0.76$ mag. We therefore conclude that our separation of younger and older pixels is reasonable, at least to first order. We will perform several more checks to confirm that this separation is appropriate (see below). At this point and at the present resolution, we do not see any special features indicating possible pixels dominated by the light from "extremely" young stellar populations (i.e., $t \lesssim 10$–100 Myr, see Fig. 2). Considering the effect of light-blending, the light from extremely young stellar populations would most likely be diluted, and hence the separation of pixels simply into younger and older pixels seems to be sufficient for this galaxy (and galaxies viewed at similar linear resolution).

Fig. 4b shows the spatial distribution of the younger and older pixels selected in Fig. 4a. The *Spitzer*/IRAC 8.0 μm PAH emission — an indicator of nearby SF-activity (e.g., Helou et al. 2004; Calzetti et al. 2005, 2007) — is overplotted in dotted contours. The distributions of younger pixels and 8.0 μm PAH emission do not exactly overlap, but are shifted slightly with respect to one another. Since the directions of these shifts are not constant, they are not the result of astrometric error in the World Coordinate System (WCS) of the images, but are genuine features, as shown by Calzetti et al. (2005). Analysis of the PAH emission and its distribution relative to SF-regions is beyond the scope of this paper, and will be deferred to a future paper. The most important result obtained from Fig. 4b is that — while no coordinate information is used to select the younger pixels in Fig. 4a — the selected pixels are grouped to-

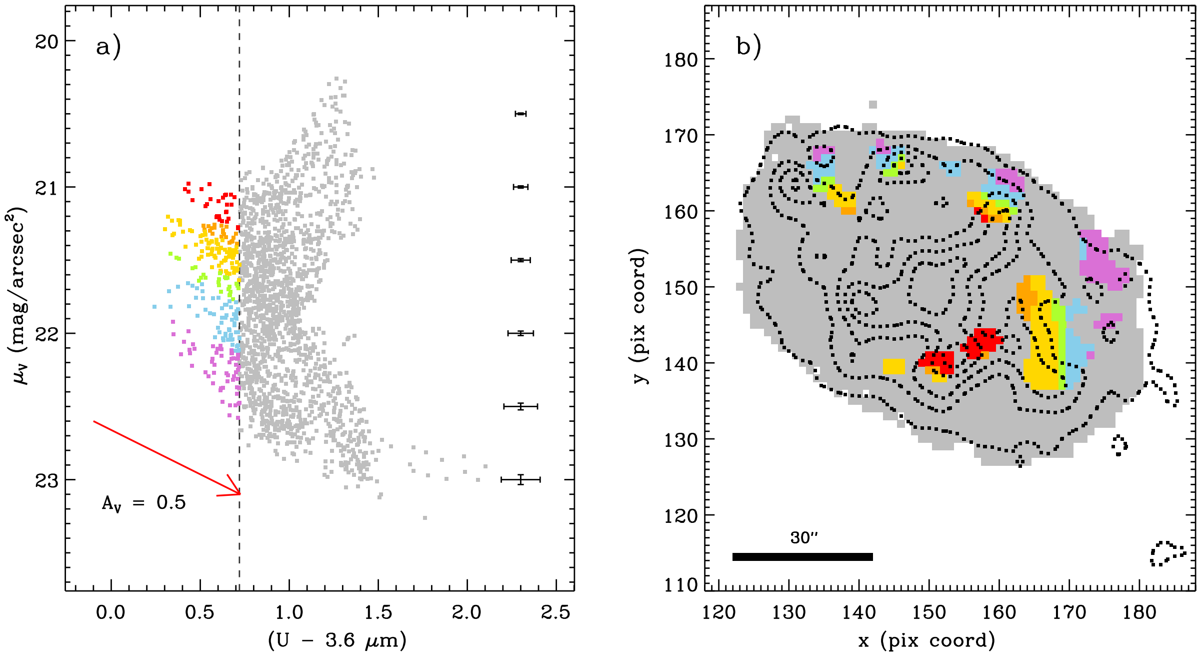

FIG. 4.— *a*) A pCMD of μ_V vs. $(U-3.6\,\mu\mathrm{m})$ for observed images. The pixels dominated by the light from younger stellar populations ("younger pixels") with $(U-3.6\,\mu\mathrm{m}) \lesssim 0.72$ mag are plotted in different colors according to the branch-like feature (see text) that they appear to be part of. The average uncertainty as a function of magnitude is indicated by the error bars along the right side of this panel. A reddening vector with $A_V = 0.5$ mag arcsec^{-2} is plotted at the lower left. *b*) Spatial distribution of the color-coded and light gray pixels selected in (*a*). Dotted contours trace the *Spitzer* 8.0 μm PAH emission. The younger pixels form *contiguous* regions; they are *not* randomly distributed. Different branch-like features in panel (*a*) correspond to regions at both systematically different galactocentric radius and with systematically different PAH emission. The younger pixels on the red-coded branch correspond to regions with strong PAH emission, and likely significant A_V, that are also relatively close-in; the purple pixels are faint at 8.0 μm, suffer little extinction, and are found at larger distances from the center.

gether into cohesive regions that coincide, or are close to peaks in the IRAC 8.0 μm emission. Moreover, different branch-like features in Fig. 4a turn out to correspond to regions at both systematically different distances from the galaxy center and systematically different PAH surface brightness. The younger pixels that form the high-surface brightness (μ_V) feature that is color-coded red in Fig. 4a originate mostly from two regions that are located near one of the strongest peaks in the 8.0 μm emission and likely suffer significant extinction. Their high surface brightness appears mostly due to the relatively small distance from the galaxy center and exponential decline in surface brightness of the disk of NGC 959 (e.g., Héraudeau & Simien 1996; Taylor et al. 2005). Younger pixels on progressively lower surface brightness features (color-coded in order: orange, gold, green, blue and purple) correspond to regions with progressively larger distance from the center and fainter PAH emission (smaller A_V).

To further confirm that our selection of the younger pixels is *not* a random result, we also visually compare Fig. 4b to color composite images of NGC 959. Fig. 5 shows *UVR* color composites at two different spatial resolutions. Both are composed from the same *U*-, *V*-, and *R*-band images observed at the VATT (Taylor et al. 2005). Fig. 5a is presented at the original pixel-scale of 0.″37 pixel^{-1}, with the PSFs in all images matched to ∼1.″3 FWHM. In Fig. 5b, the pixel-scale and resolution were matched to that of the *GALEX* NUV image, i.e., 1.″5 pixel^{-1} and 5.″3 FWHM. *Spitzer*/IRAC 8.0 μm contours (green) are overlaid in the latter image for a comparison to the pixel-map (Fig. 4b). We find that the spatial distribution of the selected *younger* pixels clearly follows that of *bluer* regions in NGC 959.

3.4. *Selecting the Theoretical V-to-3.6 μm Flux Ratio*

Having separated the "younger" and "older" pixels, we now want to estimate the theoretical extinction-free flux ratio for each pixel. As mentioned above, however, the theoretical β_V value cannot be simply selected from Fig. 2, due to the smoothing over stellar populations and subsequent blending of light. For pixels dominated by the light from older stellar populations, this should not be a major problem, since their theoretical flux ratios do not change much with age (see Fig. 2). The problem is the effect on pixels dominated by younger stellar populations. While a young SSP has a theoretical flux ratio of ∼5 (or up to ∼11 for an extremely young stellar population), the extinction-free β_V value for mixed stellar populations depends strongly on how large a fraction of the light originates from underlying and neighboring older stellar populations. Since we cannot measure the exact fractions of light from younger and older stellar populations, we have to find another way to estimate theoretical β_V values.

We first calculate the flux ratio of the observed *V* and 3.6 μm images for each pixel to characterize the effects of light-blending. The result is plotted in Fig. 6, where the white-colored histogram represents the distribution of β_V values for the pixels dominated by the light from older stellar populations ("older" pixels), and the gray-colored histogram for those dominated by the light

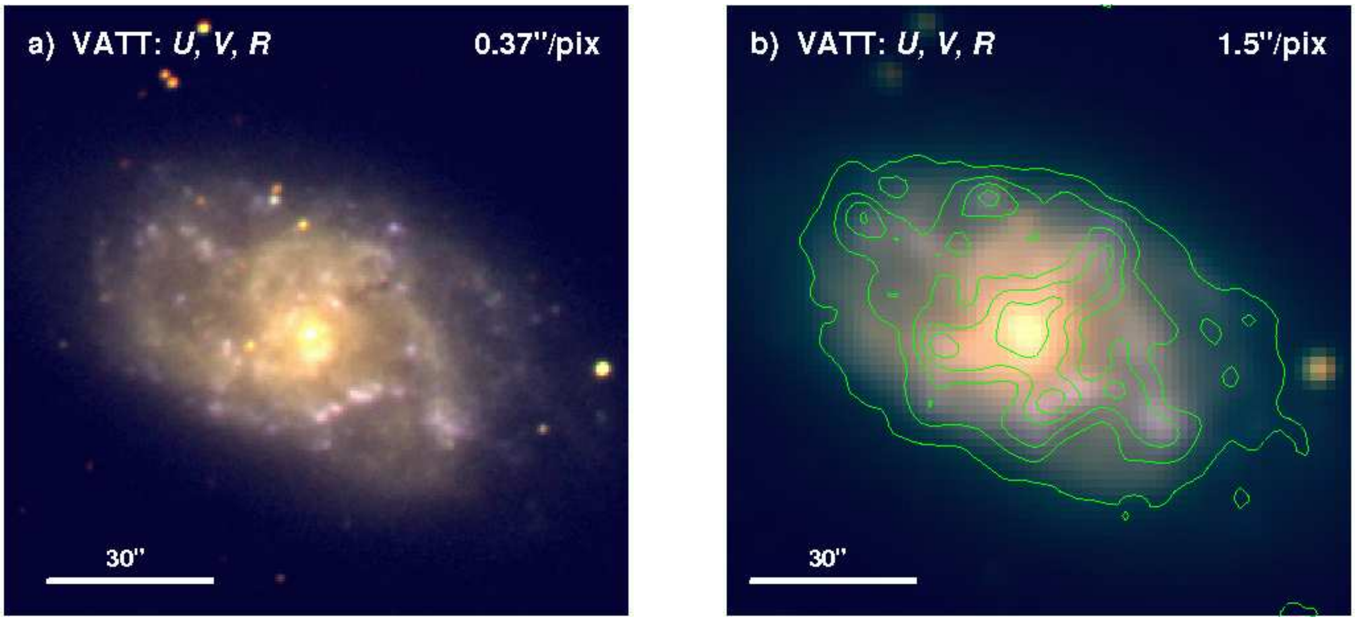

FIG. 5.— *UVR* color composite images of NGC 959 at two different spatial resolutions. *a*) A color composite image constructed at the original pixel-scale of the VATT CCD, $0\farcs37$ pixel^{-1} with a seeing of $1\farcs3$ FWHM. Dust lanes and stellar populations with different color are readily discernable in this image. *b*) A color composite image constructed from images that are resampled to the *GALEX* pixel-scale of $1\farcs5$ pixel^{-1}, and convolved to the *GALEX* PSF of $\sim 5\farcs3$ FWHM. IRAC $8.0\,\mu$m emission is indicated by green contours. Compared to the higher resolution image, dust lanes and stellar populations in this lower resolution image are not as evident. However, the blue young stellar populations remain clearly visible in the lower resolution image.

from younger stellar populations ("younger" pixels). The older pixels have a peak around $\beta_V \simeq 1.0$ with a secondary peak, or a shoulder, at $\beta_V \simeq 1.25$. This confirms our assumption that light-blending has only a minor effect on older pixels. The younger pixels display a peak at $\beta_V \simeq 1.32$, which is much lower than the theoretical ratio ($4 \lesssim \beta_V \lesssim 7$, see Fig. 2). This indicates that younger pixels are significantly affected by the light from underlying and neighboring older stellar populations. An important feature of the distribution for the younger pixels is that the observed range of β_V values is narrow and concentrated within $0.9 \lesssim \beta_V \lesssim 1.6$. This implies the effect of light-blending is rather uniform and consistent for these pixels. Stated differently, the contaminating older stellar population is distributed much more smoothly than the younger stellar population (see Fig. 5, Fig. 13 and Figs. 15–17).

Another important feature of Fig. 6 is that the tail of the distribution toward lower β_V values is larger than the tail toward higher values. Since dust extinction is the primary cause for the reduction of the V-band flux, the pixels with anomalously low β_V values are most likely located in the high-extinction regions within the galaxy. While both groups of pixels have low-β_V tails, the relative size of the tail, compared to the size of the main distribution, is much larger for the younger pixels. This indicates that dust extinction is more significant for the younger pixels.

Because interstellar dust is usually concentrated in relatively small regions (e.g., Deo et al. 2006) — while most other regions suffer minimal dust extinction — we should be able to estimate the intrinsic dust-free V-to-$3.6\,\mu$m flux ratio, $\beta_{V,0}$, for both stellar populations from Fig. 6. While the peak of the distribution for the older pixels is at $\beta_V = 1.04$, this value occurs toward the lower end of the distribution. A statistical analysis with 2σ clipping shows that the mean is at $\beta_{V,0} = 1.10$ with a standard deviation of 0.14. Even though the exact value of the intrinsic flux ratio varies from pixel-to-pixel due to the different stellar population components in each pixel, we adopt this value of $\beta_{V,0} = 1.10 \pm 0.14$ as the dust-free flux ratio for the older pixels. Unlike the older pixels, the β_V distribution of the younger pixels is more asymmetric, with a much larger tail toward lower β_V values. After 1σ clipping, the statistical mean is $\beta_V = 1.29$, which is smaller than the peak value of $\beta_V = 1.32$. Because younger stellar populations are more affected by dust than older stellar populations, which is also apparent from the much larger and wider lower-β_V tail, we elected to use $\beta_{V,0\_\rm OB} = 1.32\,^{+0.09}_{-0.15}$ (the peak β_V value) as the extinction-free flux ratio for the younger pixels. The added subscript, OB, indicates that the value is for the pixels dominated by the light from younger stellar populations, but does not imply that such pixels have no light contributed by older stellar populations.

3.5. *Calculating the Flux Difference*

Having determined appropriate extinction-free flux ratios, the next step is to calculate the V-band flux difference, Δf_V, for each pixel. Using the theoretical flux defined in equation (2), the flux difference is calculated as:

$$\Delta f_V = [f_V - (\beta_{V,0} \times f_{3.6\,\mu\rm m})]\,, \tag{4}$$

where, f_V and $f_{3.6\,\mu\rm m}$ are the observed pixel-fluxes in the optical V and IRAC $3.6\,\mu$m bands, and $\beta_{V,0}$ is the estimated extinction-free flux ratio. The distribution of Δf_V values is shown in Fig. 7 for both younger and older pixels. The solid histograms are for the Δf_V values calculated from our adopted values for $\beta_{V,0}$, while the dashed (dotted) histograms are computed for $\beta_{V,0}$ values at the upper (lower) bound of the quoted 1σ uncertainty range

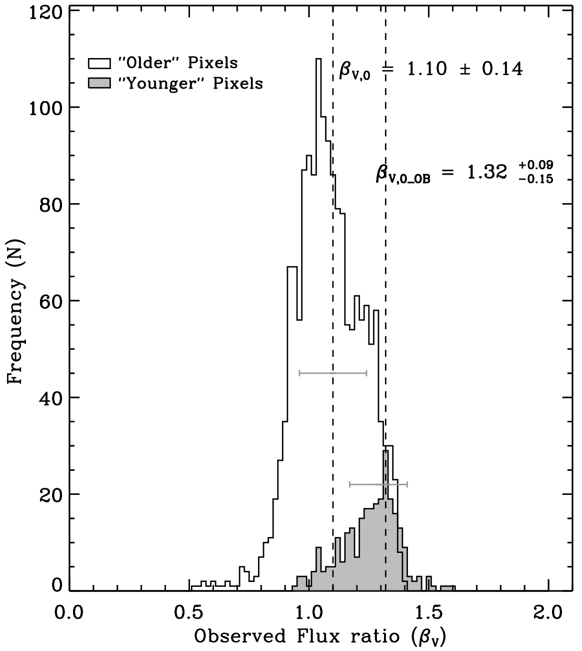

FIG. 6.— Histograms of observed V-to-3.6 μm flux ratio, β_V, for individual pixels dominated by the light from older stellar populations ("older pixels") and younger stellar populations ("younger pixels"), as selected in Fig. 4. For both populations, the low-ratio tail of the distribution — presumably due to dust extinction — is more extended than the tail on the high-ratio side. We adopt an extinction-free flux ratio, $\beta_{V,0}$, of 1.10 ± 0.14 for the older pixels and of $1.32\,^{+0.09}_{-0.15}$ for the younger pixels. Once 2σ clipped mean and peak values are selected for older and younger pixels, respectively, corresponding uncertainties are determined from the FWHM of β_V distributions. Because of light-blending from different populations contributing to the flux in a given pixel, the β_V values for the young stellar population are significantly reduced compared to those calculated for SSP models in Fig. 2.

in Fig. 6. While Fig. 6 shows simply the level of the V-band flux relative to the flux in 3.6 μm filter, Fig. 7 shows the *absolute* difference between the observed and estimated theoretical V-band pixel-fluxes. Regardless of the selection of $\beta_{V,0}$, both histograms — for both younger and older pixels — show that the number of pixels with positive Δf_V goes to zero quickly, and that there are distinct tails extending to large negative values of Δf_V. For the younger pixels, the effect of the uncertainty in the selection of $\beta_{V,0}$ is small (i.e., the three histograms show similar distribution in Fig. 7b). The older pixels, however, are affected more (Fig. 7a). Since older stellar populations tend to have less dust intermixed, and hence suffer less extinction, the dashed histogram for the larger value of $\beta_{V,0}$ produce an excess of pixels with large values of A_V. On the other hand, the dotted histogram for the smaller value of $\beta_{V,0}$ will produce many pixels with an unphysical excess of visual flux, indicating that this value must be a robust lower bound on $\beta_{V,0}$. This confirms that $\beta_{V,0} = 1.10$ is a reasonable and appropriate value for the older pixels.

Next, we check the spatial distribution of the calculated Δf_V values. If the distribution of negative Δf_V follows genuine galactic features, such as SF-regions, spiral arms, and PAH emission, then this strengthens our argument that our method largely traces the dust extinction. The spatial distribution of Δf_V is shown as a pixel-coordinate map in Fig. 8, with the IRAC 8.0 μm emission overlaid as dotted contours. This map demonstrates that the distribution of Δf_V values is not random at all, but closely associated with genuine galactic structures. Visual comparison of this map to the color composite image in Fig. 5b confirms that pixels with a large deficiency of observed V-band flux are not simply corresponding to pixels appearing darker (lower surface brightness). Instead, pixels with $\Delta f_V < 0$ are distributed around the regions that appear bluer, as well as near the center of the galaxy. The higher resolution image of Fig. 5a shows that some pixels with larger negative values of Δf_V (darker gray in Fig. 8) trace the visible dust lanes, seen in silhouette, and the bluer SF-regions. This demonstrates that even though some of the dust is not visually conspicuous (as in the lower resolution image in Fig. 5b), our method is capable of estimating dust extinction and its spatial distribution from observations in only two broadband filters — with a third filter (U-band) serving only to robustly separate younger pixels from older pixels (Figs. 3 and 4). Since regions with visible or plausible dust content are recovered well by our method, this gives us confidence that regions for which this method indicates a low dust content could also be real.

Before we proceed to estimate the amount of dust extinction in each pixel, there is one more check that we must perform to support our separate treatment of the younger pixels. The main panel of Fig. 9 shows a map of Δf_V for the younger pixels for our adopted value of $\beta_{V,0\_\mathrm{OB}} = 1.32$, while the inset shows the result when these pixels are treated as older pixels with $\beta_{V,0\_\mathrm{OB}} = \beta_{V,0} = 1.10$. The lighter shade of gray of the pixels in the inset panel indicates that most of them have positive Δf_V, suggesting that the observed V-band flux is equal to or larger than expected from the 3.6 μm data, i.e., that the younger pixels miss either no V-band flux or show an unphysical *excess* of observed V-band flux. Since young stellar populations are usually associated with relatively large amounts of dust (e.g., van Houten 1961; Knapen et al. 1991; Regan et al. 2004; Barmby et al. 2006), a value of $\beta_{V,0} = 1.10$ is clearly too small for the younger pixels. Our separate treatment of the younger pixels, adopting $\beta_{V,0\_\mathrm{OB}} = 1.32\,^{+0.09}_{-0.15}$ as outlined above, is therefore appropriate. For that larger value of $\beta_{V,0}$, the younger pixels are found to suffer small-to-moderate amounts of extinction by dust, consistent with the known presence of dust at or near these regions of recent star formation and producing consistent results with previous studies.

3.6. *Measuring the Dust Extinction*

We can now estimate the most likely amount of dust extinction in each pixel. With $\beta_{V,0} = 1.10$ (and $\beta_{V,0\_\mathrm{OB}} = 1.32$) and AB-magnitude zeropoint, $V_{\mathrm{zp,AB}} = 48.59$ mag, equation (3) becomes:

$$A_V = m_V - [-2.5 \log(\beta_{V,0} \times f_{3.6\,\mu\mathrm{m}}) - V_{\mathrm{zp,AB}}] . \quad (5)$$

We cannot simply apply equation (5) to all pixels, however, since some pixels have $\beta_V > \beta_{V,0}$ (see Fig. 6) and $\Delta f_V > 0$ (see Fig. 7), i.e., seemingly implying an unphysical negative dust extinction, A_V. Because the $\beta_{V,0}$ value is the *estimated* extinction-free flux ratio, rather than the

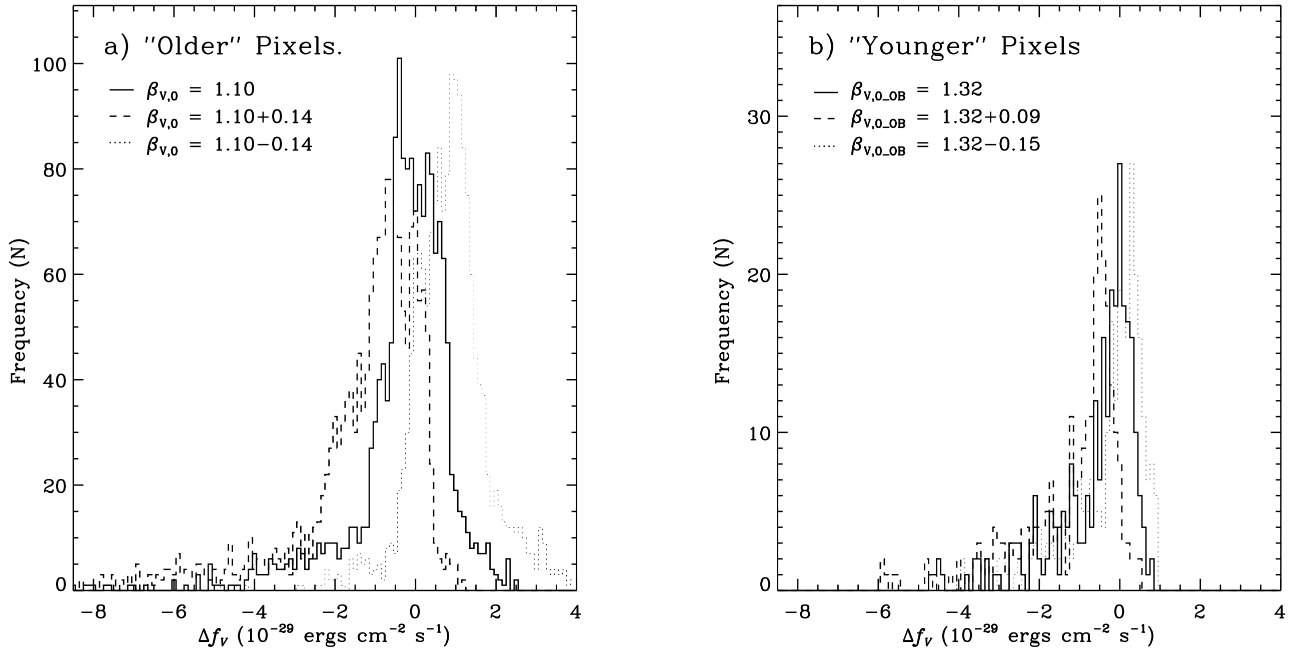

Fig. 7.— Histograms of Δf_V, the difference between the observed and theoretical V-band flux for selected pixels with light dominated by (*a*) older and (*b*) younger stellar populations. In each panel, the solid histogram is for the adopted value of $\beta_{V,0}$, while the dashed (dotted) histogram assumes a value for $\beta_{V,0}$ that corresponds to the upper (lower) bound of the uncertainty range determined in Fig. 6.

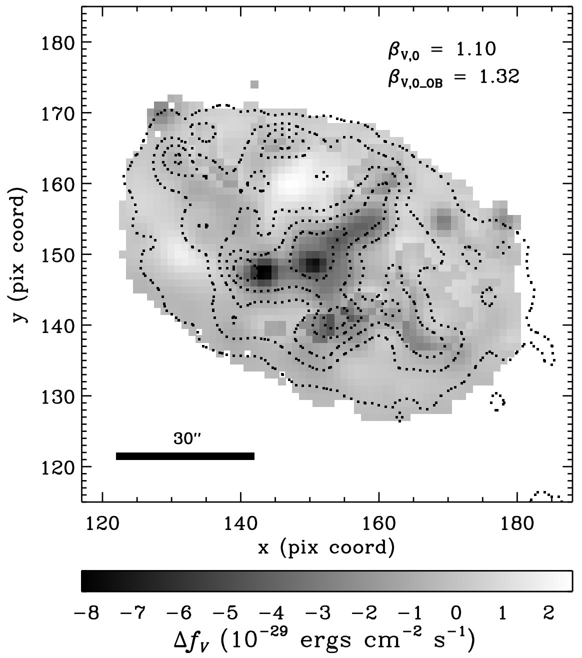

Fig. 8.— Pixel map of the flux difference, Δf_V, rendered at the resampled pixel-scale of 1.″5 pixel^{-1}. Darker gray-scale levels indicate a larger deficiency of observed V-band flux compared to the modeled intrinsic flux. Black dotted contours trace the IRAC 8.0 μm PAH emission. While it is hard to visually trace the distribution of dust in Fig. 5b, the locations of the dust lanes in Fig. 5a generally agree with the distribution of the flux-deficient pixels in the present figure.

true dust-free ratio, it is possible that some pixels have an observed β_V value that is larger than $\beta_{V,0}$. We therefore have to be careful how we treat these pixels in our analysis.

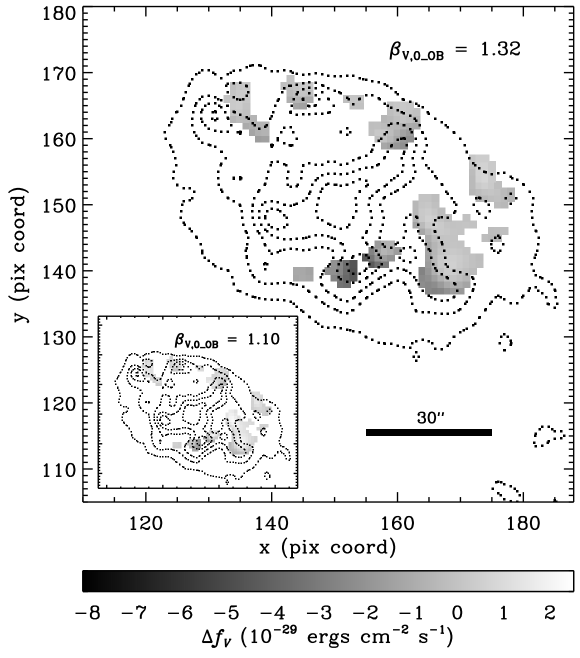

Fig. 9.— Comparison of the flux difference, Δf_V, inferred for pixels dominated by younger stellar populations. The main panel shows the result when the younger pixels are treated separately, adopting $\beta_{V,0\_OB} = 1.32$. Here, most pixels show that they are missing V-band flux, as expected. The inset panel shows the result for no such special treatment (i.e., assuming $\beta_{V,0\_OB} = \beta_{V,0} = 1.10$, as for pixels dominated by old stellar populations). Here, most of the younger pixels show an unphysical *excess* of observed V-band flux. Black dotted contours trace 8.0 μm PAH emission.

As mentioned above, the pixels with positive Δf_V (Fig. 8) appear darker than neighboring regions in the color composites of Fig. 5. Considering also that the

8.0 μm PAH emission is weak in these regions (i.e., these pixels are surrounded by outer 8.0 μm contours with large spacing between neighboring contours), these positive Δf_V pixels are not caused by SF-activity, but are most likely the result of underestimating the intrinsic $\beta_{V,0}$ value. The actual amount of dust extinction might also be minimal or zero ($A_V \simeq 0$) for these pixels. We adopted a single $\beta_{V,0}$ for younger and for older pixels, yet the intrinsic flux ratio for each pixel will vary slightly based on different factors. As a result, some pixels with positive Δf_V are expected, even in the absence of noise. For our adopted $\beta_{V,0}$ of 1.10 (1.32) for older (younger) pixels, most pixels with excess flux have $\Delta f_V \lesssim 1.0 \times 10^{-29}$ ergs cm^{-2} s^{-1}, and only a very small fraction has an excess as large as $\sim 2.0 \times 10^{-29}$ ergs cm^{-2} s^{-1} (see Fig. 7). In the following, we will therefore assume that these pixels suffer no extinction, i.e., that $A_V = 0$ mag arcsec^{-2}.

3.6.1. *Impact of the Uncertainty in $\beta_{V,0}$*

Since neither the relationship between A_V and Δf_V nor the relationship between Δf_V and β_V is linear, the 1σ errors in the estimated extinction-free flux ratios ($\sigma_{\beta_{V,0}} = \pm 0.14$ and $\sigma_{\beta_{V,0\_{\rm OB}}} = +0.09$ & -0.15) cannot be simply converted to corresponding σ_{A_V} values. Instead, we will assess *how* the distribution and values of A_V change, as we vary the estimated dust-free flux ratio from the adopted value of $\beta_{V,0}$ to $\beta_{V,0} \pm \sigma_{\beta_{V,0}}$.

Fig. 10 shows the spatial distribution of the estimated dust extinction, A_V, for each pixel in NGC 959, for two sets of theoretical extinction-free flux ratios. Fig. 10a shows the distribution of A_V inferred for our adopted $\beta_{V,0}$ values of 1.10 and 1.32 for older and younger pixels, while Fig. 10b shows the result for $\beta_{V,0}$ values set at the higher end of the uncertainty range (i.e., $\beta_{V,0} = 1.24$ and 1.41, respectively). The mean and maximum dust extinction for all pixels in Fig. 10a (Fig. 10b) are $A_{V,\rm mean} = 0.064$ (0.15) and $A_{V,\rm max} = 0.80$ (0.93) mag arcsec^{-2}. As expected, the dust-extinction map (not shown) for the lower limit, $\beta_{V,0} - \sigma_{\beta_{V,0}}$, is covered mostly by $A_V = 0$ pixels. These results are summarized in Table 1, where the last column indicates the fraction of pixels with $A_V = 0$ mag arcsec^{-2} in the image.

Even though the estimated $\beta_{V,0}$ value changes, Fig. 10 shows that the distribution of dust extinction follows the structures of the galaxy and the 8.0 μm contours. Fig. 10 and Table 1 also show that the effect of varying the theoretical $\beta_{V,0}$ value is not equal to simply adding or subtracting a constant value ΔA_V to the dust-extinction values calculated for our adopted value of $\beta_{V,0}$. As $\beta_{V,0}$ change from 1.10 and 1.32 (Fig. 10a) to 1.24 and 1.41 (Fig. 10b), some pixels near pixels with $A_V \gtrsim 0$ mag arcsec^{-2}, which originally were deemed extinction-free, now suffer a slight amount of dust extinction. Other pixels that are further away, e.g., pixels in areas that are faint at 8.0 μm, stay at $A_V = 0$ mag arcsec^{-2}. This confirms our assumption that these pixels have minimal or no dust extinction.

3.6.2. *Analysis at Higher Spatial-Resolution as Confirmation*

While individual dust features usually are small-scale structures, our initial analysis was performed at the low spatial resolution of the *GALEX* NUV image. To determine if our result is a true measure of dust extinction or not, we repeat the same analysis with *higher* spatial resolution images, using only U, V, and IRAC 3.6 μm images. Since the 3.6 μm image has the coarsest pixel scale of 1″.2 pixel^{-1} and a PSF with $\sim$2″.2 FWHM, the ground-based U- and V-band images are registered, resampled, and convolved to match the orientation, pixel scale, and resolution of the 3.6 μm image. Fig. 11 shows the distribution of estimated A_V values at this higher spatial resolution. The 8.0 μm contours are overplotted at the native IRAC resolution of $\sim$2″.3 FWHM.

An important difference between the two spatial resolutions is that, while the maximum dust extinction is $A_{V,\rm max} \simeq 0.8$ mag arcsec^{-2} in Fig. 10a, $A_{V,\rm max}$ in Fig. 11 reaches $\sim$2.3 mag arcsec^{-2}. This jump in A_V value is expected, since the coarser *GALEX* PSF smoothes out the effect of dust extinction and reduces the averaged A_V for each pixel. Since the ratio of the effective areas of the *GALEX* NUV and *Spitzer* 3.6 μm PSFs is (5″.3/2″.2)$^2 \simeq 6$, the typical extinction per pixel should change, to first order, by $\sim$1.9 mag arcsec^{-2}. Other factors, such as uncertainties in estimating $\beta_{V,0}$ and blending of light from structures that are unresolved with the coarser while resolved with the smaller PSF, also play a role. The observed shift in A_V of $\Delta A_V \simeq 1.5$ mag arcsec^{-2} is therefore broadly consistent, while the 0.4 mag arcsec^{-2} difference illustrates the effects of the clumpiness of stars and dust on scales of 2″.2–5″.3 ($\sim$110–250 pc at the distance of NGC 959). The higher spatial resolution images are better at tracing smaller dust features and their higher extinction values within a single pixel. Nonetheless, the overall distribution of dust extinction is similar in Figs. 10 and 11. While the fine details of the measurable dust extinction and its spatial distribution depend on the resolution, both extinction maps trace the 8.0 μm PAH emission and trace genuine galactic structures.

In conclusion, from the series of tests described above, we find that the two-dimensional distribution of dust extinction can, indeed, be reliably estimated by our pixel-based method and the observed V-to-3.6 μm flux ratio.

3.6.3. *Interesting Regions*

Having produced maps of the spatial distribution of dust extinction in NGC 959, we now discuss some of the most interesting dust features in Fig. 10 (and Fig. 11). While the distribution of regions with larger A_V closely traces the SF-regions, a not previously identified bar, and arm-like structures, there are several regions that draw our attention. These are: (1) a compact region at the Northeast edge (NE; upper-left) of NGC 959 that appears to suffer very high extinction; (2) another such high-extinction region at the Northwest edge (NW; upper-right); and (3) an extended area of moderate dust extinction along the Southeast (SE; bottom), rim of the galaxy. Since all of these features are also visible in Fig. 11, these must be real features. To visually confirm small-scale dust features in NGC 959, and check their interpretation as genuine galactic features as opposed to chance superpositions of unrelated objects, we created another color composite from Archival *HST*/WFPC2 F450W, F606W, and F814W images, shown in Fig. 12. The two circles in

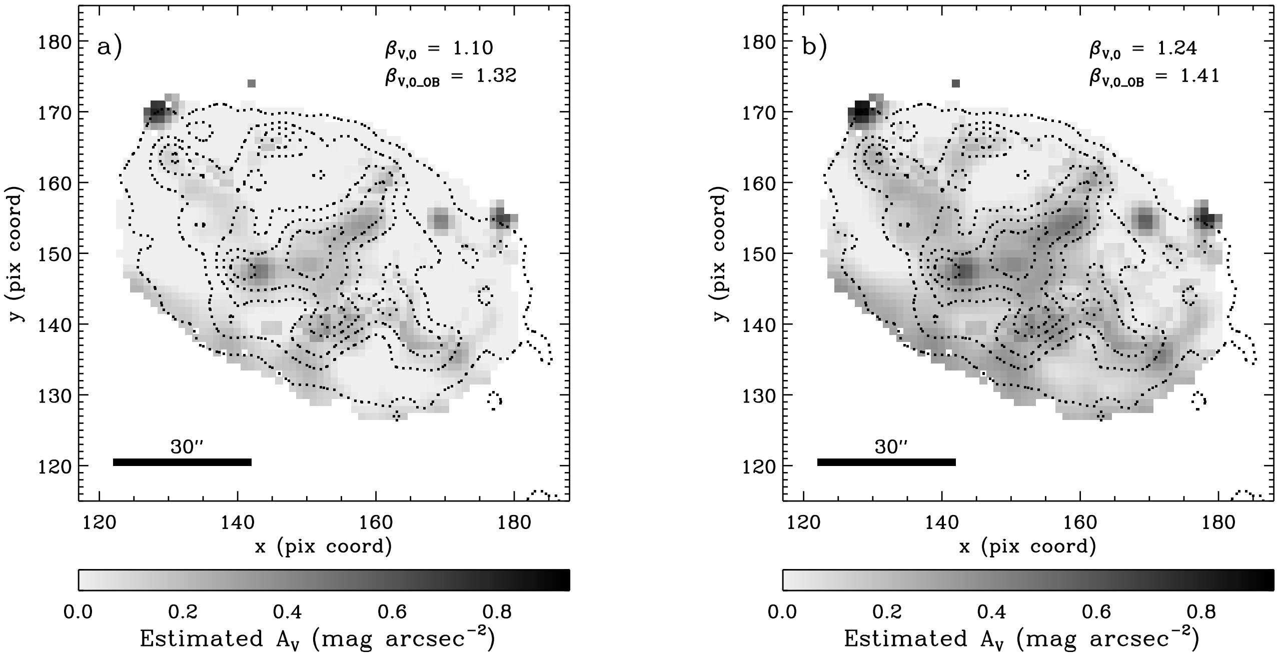

Fig. 10.— Spatial distribution of A_V, inferred for $\beta_{V,0}$ values of (*a*) 1.10 and 1.32 (mean), and (*b*) 1.24 and 1.41 (upper limit), for older and younger pixels, respectively. The same gray-scale is used for both (*a*) and (*b*). The pixels with the lightest shade of gray have no detectable extinction ($A_V = 0$ mag arcsec^{-2}). The darkest pixels have a visual extinction $A_V \simeq 0.8$ mag arcsec^{-2} in (*a*) and $\simeq 0.93$ mag arcsec^{-2} in (*b*). Dotted contours trace the 8.0 μm PAH emission. These extinction maps indicate that the higher extinction coincides with SF-regions that appear blue in the color composite images (see Fig. 5), as well as with several dust features visible in Fig. 5a.

TABLE 1
Dust Extinction Based on Different $\beta_{V,0}$ Values

Selected $\beta_{V,0}$ Level	$\beta_{V,0}$	$\beta_{V,0\_\mathrm{OB}}$	A_{V_mean} [a] (mag arcsec^{-2})	A_{V_max} (mag arcsec^{-2})	% of pixels with $A_V = 0$
Adopted $\beta_{V,0}$	1.10	1.32	0.064	0.80	45.0%
Upper $(+\sigma)$	1.24	1.41	0.15	0.93	16.4%
Lower $(-\sigma)$	0.96	1.27	0.015	0.63	83.1%

[a] Mean A_V value of all pixels analyzed for the galaxy.

this image mark regions (1) and (2).

The NE high-A_V region, region (1), is centered around pixel coordinates $[x, y] \simeq [128, 169]$ in Fig. 10. Even though nothing conspicuous is visible in the low-resolution color composite (Fig. 5a), the *HST* image (Fig. 12) reveals a compact, bright red source at the center of the marked region. Without morphological indicators, multi-filter photometry, or spectroscopic information for this particular object, it is hard to decide whether this is a reddened stellar population within NGC 959's disk, or a background (foreground) object that is visible through (against) the disk. We do note, however, that the color of this object is very similar to that of the edge-on background galaxy that is visible at the bottom left of Fig. 12. Region (2) is located in the NW corner of the galaxy around $[x, y] \simeq [178, 155]$. There is no F606W coverage for this region in Fig. 12, but there is no object discernable in the other two *HST* filters. At present, we lack sufficient information to establish if these regions are truly associated with NGC 959. Until further evidence is obtained, we will treat these regions as a part of the galaxy.

The pixels comprising feature (3), the moderate-extinction region running along the SE rim of the galaxy disk, initially did not show up as having particularly large-negative Δf_V values (see Fig. 8). Once the dust extinction is calculated, these pixels do stand out with low–moderate A_V values, indicating the presence of an extended dust structure. The higher-resolution dust extinction map (Fig. 11) also shows that the pixels in this region suffer higher dust extinction than inferred for the opposite (NW) rim of the galaxy. Visual comparison to Fig. 12 confirms that a faint dust lane runs along the SE rim, apparently tracing an outer spiral arm or armlet. This shows that our dust extinction measurement using the V-to-3.6 μm flux ratio is sensitive to even low amounts of dust extinction per resolution element, whether inherently smoothly distributed or resulting from a small filling factor.

3.6.4. *Correcting for Dust Extinction*

Finally, using the calculated A_V values for each pixel, we correct the observed V-band image of NGC 959 to reveal the true underlying stellar populations. The observed (uncorrected) and extinction-corrected images are shown at *GALEX* resolution in the top panels of

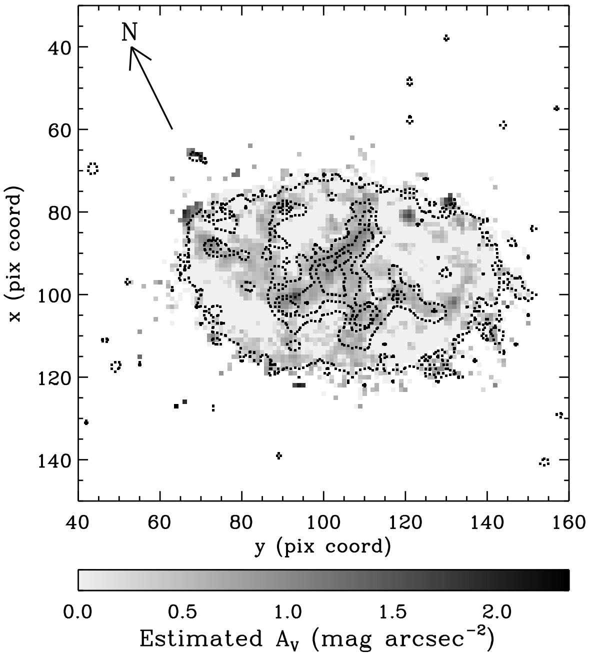

FIG. 11.— Distribution of dust extinction at the (higher) spatial resolution of the *Spitzer*/IRAC 3.6 μm image (1.″2 pixel^{-1} and ∼2.″2 FWHM). The dotted contours trace 8.0 μm PAH emission at a native resolution of ∼2.″3 FWHM. This map is presented in the instrument coordinate system, oriented as indicated at the upper left.

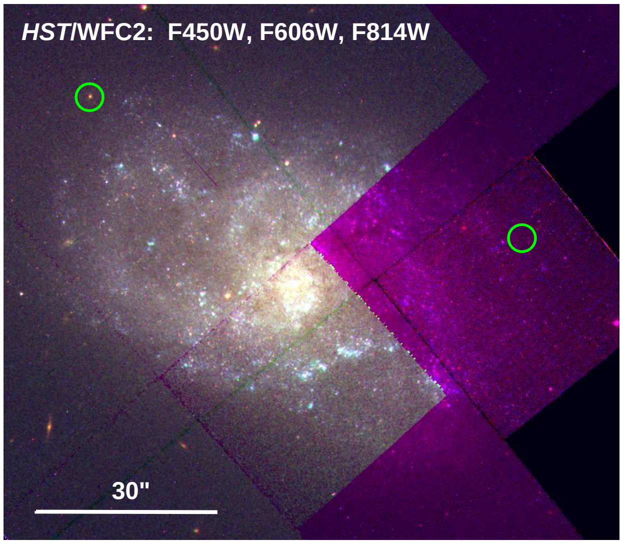

FIG. 12.— Color composite of Archival *HST*/WFPC2 F450W, F606W, and F814W images. The green circles indicate the two regions with high apparent A_V in Fig. 10. While there is no object evident within the right green circle, the circle in the upper left corner contains a red object. Along the southern rim of NGC 959, a faint dust lane is discernable that appears to trace an outer arm. The typical extinction along this dust feature is $A_V \simeq 0.3$–0.4 mag arcsec^{-2} in Fig. 10.

Fig. 13, using the *same* gray-scale lookup table. The surface brightness distribution before extinction correction (Fig. 13a) has lower contrast overall and fewer high-contrast features. Most conspicuous after applying our dust correction (Fig. 13b) is that bluer regions in the color composite of Fig. 5b become much more prominent, while other galactic structures (particularly the central bulge) also become better defined. Especially for areas SE (centered on $[x, y] \simeq [142, 148]$) and NW ($[x, y] \simeq [159, 155]$) of the galaxy center, the V-band surface brightness becomes much brighter in areas where dust lanes are evident in the color composites (Fig. 5a and Fig. 12). The bottom two panels show the observed *Spitzer*/IRAC 3.6 μm and 4.5 μm images (Figs. 13c and 13d), which trace the distribution of the underlying older stellar populations (e.g., Regan et al. 2004; Willner et al. 2004). These MIR images and the *extinction-corrected* V-band surface brightness distribution show excellent qualitative agreement. Therefore, as Regan (2000) did with optical–NIR images and radiative transfer modeling, we successfully corrected the dust extinction with images in only two filters (V and 3.6 μm) — with a U-band image serving only to robustly separate pixels dominated by the flux from younger stellar populations from those dominated by older stellar populations.

4. APPLICATION TO OTHER FILTERS

Given the amount of visual dust extinction, A_V, in each pixel, we can calculate the extinction in any other filter. The extinction in a given filter depends on its throughput as a function of wavelength, as well as on the metallicity of the stellar populations of the galaxy of interest through the adopted extinction curve (e.g., Seaton 1979; Koornneef & Code 1981; Howarth 1983; Cardelli et al. 1989; Calzetti et al. 1994; Gordon et al. 2003). In a forthcoming paper (Tamura et al. 2009b, in preparation), we will use UV–MIR multi-filter dust-corrected surface photometry for a detailed analysis of the stellar populations within NGC 959.

4.1. *Extinction Curves*

In general, dust extinction increases toward shorter wavelengths. For metal-poor stellar populations — such as those in the Small Magellanic Cloud (SMC) — the dust-extinction curve is largely monotonic as a function of wavelength. The shape of the extinction curve becomes more complicated for metal-rich stellar populations. Especially the extinction at shorter wavelengths ($\lambda \lesssim 2200$ Å) may be significantly affected by the 2175 Å interstellar dust feature and the increased steepness of the UV extinction (e.g., Calzetti et al. 1994; Gordon et al. 2003, see also Fig. 14 here).

Gordon et al. (2003) compared the observations of many stars to calibrate the extinction curves — the wavelength dependent extinction relative to that at 0.55 μm — for SMC, LMC, and MW type dust. Based on Table 4 (and Fig. 10) of Gordon et al. (2003), we interpolated the published extinction curves on a finer wavelength grid. In the NIR, Gordon et al. (2003) have only one datapoint for each of the 2MASS JHK_s filters, and the SMC extinction curve in particular appears quite uncertain. To cover longer wavelengths up to the *Spitzer*/IRAC filters, in the NIR and MIR, we adopted the Galactic extinction curve of Fitzpatrick (1999), rescaled for $R = A_V/E(B-V) = 3.1$. The adopted extinction curves for SMC, LMC, and MW metallicities are plotted in Fig. 14. For wavelengths shorter than the 2175 Å interstellar dust feature, the SMC and MW type extinctions differ by ∼2 mag. The bottom panel of Fig. 14

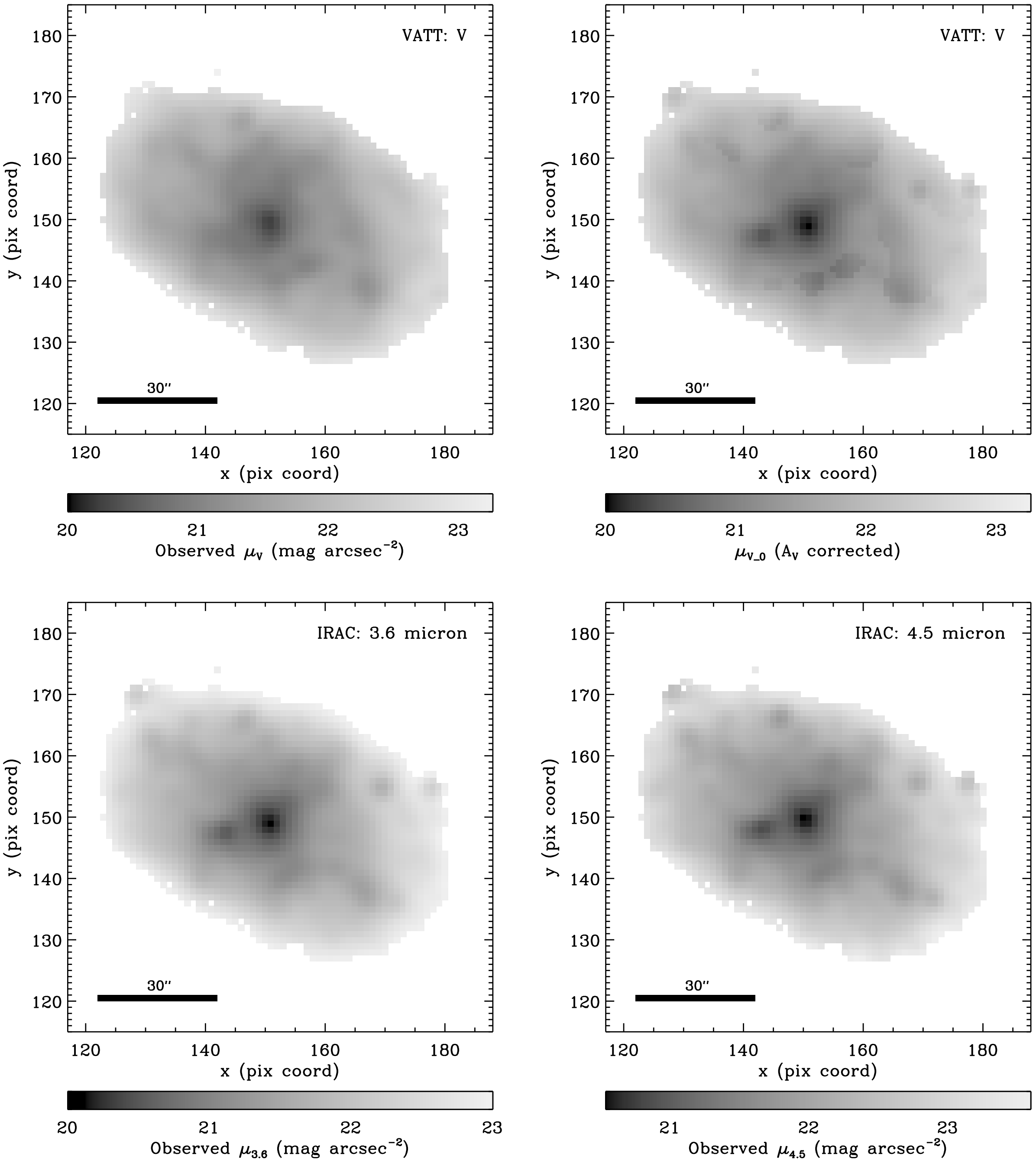
VATT: V
VATT: V
IRAC: 3.6 micron
IRAC: 4.5 micron
y (pix coord)
x (pix coord)
120
130
140
150
160
170
180
30″
20
21
22
23
Observed μ_V (mag arcsec^{-2})
μ_{V_0} (A_V corrected)
Observed $\mu_{3.6}$ (mag arcsec^{-2})
Observed $\mu_{4.5}$ (mag arcsec^{-2})

Fig. 13.— Comparison of observed (*top left*) and extinction-corrected (*top right*) V-band images and the observed *Spitzer*/IRAC 3.6 and 4.5 μm images (*bottom*) of NGC 959 at *GALEX* resolution. The MIR images are good tracers of the underlying stellar distribution. The extinction-corrected image in V displays more brighter (darker shade) pixels around blue SF-regions (see Fig. 5) and better resembles the MIR images than does the observed V-band image.

shows the relevant filter throughput curves for comparison. The amount of dust extinction in each filter, $A_{\rm filter}$, is calculated as a ratio to the extinction in V:

$$A_{\rm filter}/A_V = \frac{\int_\lambda T_{\rm filter}(\lambda)\,[A(\lambda)/A_V]\,d\lambda}{\int_\lambda T_{\rm filter}(\lambda)\,d\lambda}, \qquad (6)$$

where, $T_{\rm filter}(\lambda)$ is the throughput curve for each filter, and $[A(\lambda)/A_V]$ denotes an extinction curve (Fig. 14). Table 2 summarizes the computed dust extinction for the different extinction curves. For the 2MASS JHK_s filters, the extinction calculated from the SMC, LMC, and MW extinction curves of Gordon et al. (2003) differs significantly (indicated with asterisks in Table 2). Since the extinction at longer wavelengths is progressively insensitive to metallicity, we conclude that these values must be highly uncertain. Instead, we use the extinction curve of Fitzpatrick (1999) to provide an upper limit to the dust extinction in the filters longward of 1 μm (parenthesized values in Table 2). Since the extinction is small ($A_{\rm filter}/A_V < 0.1$), following previous stud-

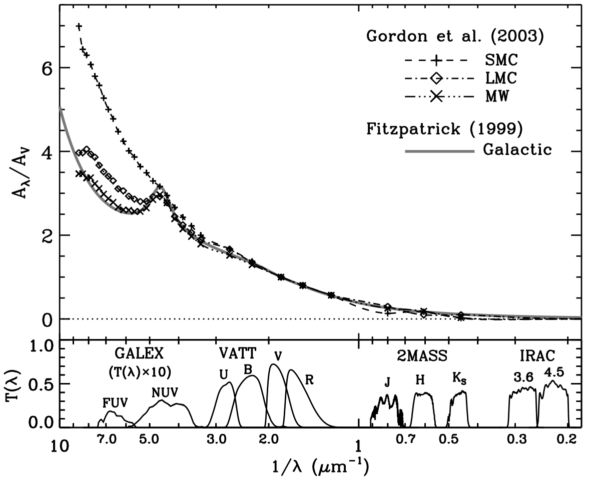

FIG. 14.— *Top panel*: Extinction curves for SMC (pluses), LMC (open diamonds), and MW (crosses) metallicity from FUV to MIR wavelengths. The smooth extinction curves were interpolated from the data points of Gordon et al. (2003). Also shown is the Galactic extinction curve from Fitzpatrick (1999), which we adopt for the NIR and MIR filters. *Bottom panel*: Total throughput curves, T(λ), for different telescope-filter combinations (see also Fig. 1). The *GALEX* filter curves were scaled up by a factor of 10 for better visibility.

ies (e.g., Fazio et al. 2004; Regan et al. 2004), we assume that there is no measurable dust extinction in the IRAC filters.

An important assumption for the extinction curves described above is that the dust is distributed in the form of a "diffuse-ISM" or in a diffuse-screen geometry, which is applicable only for nearby stars and star clusters *within* our own Galaxy. In extragalactic objects, the dust appears to be distributed in smaller clumps of much higher density (e.g., Deo et al. 2006) intermixed with the stars. Even though the effect of dust extinction is averaged (or smoothed out) within an aperture or a resolution element — a single pixel in our pixel-based analysis — the properties of dust extinction (e.g., the 2175 Å feature and the steepness of the UV-extinction curve) are governed by the actual geometry of the dust distribution within a galaxy. This means that two regions with the same *average* visual extinction A_V can have different amounts of extinction A_λ at another wavelength, either because of differences in *metallicity* or because of different *dust geometries*.

TABLE 2
DUST EXTINCTION ($A_{\rm filter}/A_V$)

Instrument & Filter	$\lambda_{\rm center}$ (μm)	x (μm^{-1})	SMC	LMC	MW
GALEX FUV	0.153	6.536	4.56	3.16	2.70
GALEX NUV	0.227	4.405	2.91	2.59	2.53
VATT U	0.360	2.778	1.65	1.64	1.50
VATT B	0.437	2.288	1.37	1.35	1.29
VATT V	0.542	1.845	1.00	1.00	1.00
VATT R	0.642	1.558	0.81	0.81	0.81
2MASS J	1.235	0.810	0.14*	0.29*	0.36* (≤0.26)
2MASS H	1.662	0.602	0.15*	0.10*	0.18* (≤0.17)
2MASS K_s	2.159	0.463	0.03*	0.09*	0.04* (≤0.11)
IRAC 3.6 μm	3.550	0.282	···	···	(≤0.06)
IRAC 4.5 μm	4.493	0.223	···	···	(≤0.04)
IRAC 5.8 μm	5.791	0.173	···	···	(≤0.03)
IRAC 8.0 μm	7.872	0.127	···	···	(≤0.02)

NOTE. — An asterisk indicates that the uncertainty is significant compared to the actual extinction values. The values in parenthesis are calculated using the Galactric extinction curve from Fitzpatrick (1999).

Two extreme cases of dust geometry are: (1) a uniform thin slab (i.e., commonly referred to as a "diffuse ISM"); and (2) dense clumps covering a small fraction of a resolution element. While we would like to perform a detailed study of the dust geometry and its effect on the extinction curve for extragalactic objects, this is beyond the scope of the present paper. Here, we briefly discuss the effects of the different dust geometries studied by Whittet et al. (2001, 2004). Whittet et al. (2001) studied a total of 27 sight-lines (stars) toward the dark clouds in the Taurus region. One of the results from their study is that $R_V = A_V/E(B-V)$ changes from a "normal" to a "dense cloud" regime once the extinction exceeds a threshold value of $A_{\rm th} \simeq 3.2$ mag. Whittet et al. (2004) subsequently studied the effect of dust geometries in detail, which included a thin "diffuse screen" and a diffuse screen with an embedded "dense cloud" (see their Fig. 1). For a detailed analysis and discussion, we refer the reader to their papers. The main effect of the "dense cloud" geometry on the extinction curve is to weaken or remove the 2175 Å extinction bump (see Fig. 5 of Whittet et al. 2004) while having little effect on the extinction curve at other wavelengths, which remains at the same level as for the mean "diffuse ISM" (Fig. 2 of Whittet et al. 2004). The extinction curves recreated from Gordon et al. (2003) and Fitzpatrick (1999), and the calculated extinction values $A_{\rm filter}/A_V$ (Fig. 14 and Table 2) are therefore treated as the upper limit to the dust extinction from different dust geometries. Since the 2175 Å feature is covered only by the *GALEX* NUV filter, the uncertainty associated with different dust geometries is assumed to be minimal in all filters except the *GALEX* NUV. Since the *GALEX* NUV filter is not used in our method, we will defer further analysis of the NUV filter to subsequent papers (Tamura et al. 2009b,c, in preparation).

4.2. *A Dust-Free View of NGC 959*

Since NGC 959 is classified as an Sdm galaxy in the RC3, we assume that it has an average metallicity between the SMC and the MW value. We therefore adopt the LMC extinction curve to estimate the extinction in filters other than V. Using the LMC extinction ratios $A_{\rm filter}/A_V$ from Table 2, we scale the V-band extinction for each pixel as:

$$A_{\rm filter} = A_V \times (A_{\rm filter}/A_V)\,, \qquad (7)$$

where, A_V was computed using equation (5). Figs. 15–17 show the *uncorrected* (left panels) and the *extinction-corrected* images (right panels) for NGC 959 from the FUV to R at *GALEX* NUV resolution. In all filters, the SF-regions become more clearly visible in the extinction corrected images. Compared to the optical V-band and the MIR 3.6 and 4.5 μm images (Fig. 13), in which the highest surface brightness is reached in the galaxy center, the brightest regions in the extinction-corrected *GALEX*

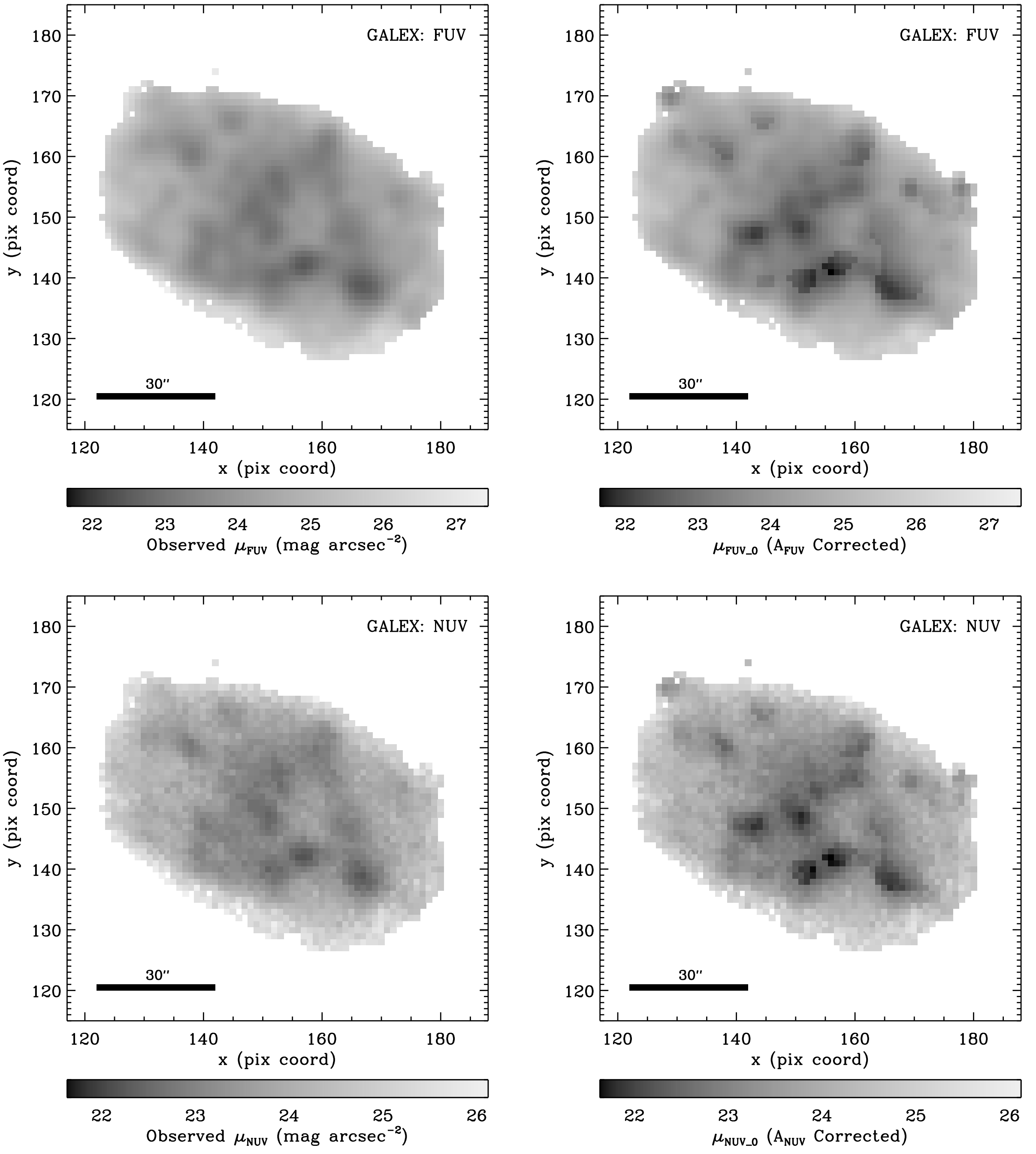
GALEX: FUV
GALEX: FUV
GALEX: NUV
GALEX: NUV
30″
y (pix coord)
x (pix coord)
120
130
140
150
160
170
180
22
23
24
25
26
27
Observed μ_{FUV} (mag arcsec^{-2})
μ_{FUV_0} (A_{FUV} Corrected)
Observed μ_{NUV} (mag arcsec^{-2})
μ_{NUV_0} (A_{NUV} Corrected)

Fig. 15.— Comparison of observed (*left*) and extinction-corrected (*right*) images in the *GALEX* FUV (*top*) and NUV (*bottom*) filters.

FUV and NUV images are distributed all over the galactic disk. Since these FUV and NUV filters are especially sensitive to young stellar populations (see Fig. 1), this indicates that most of the recent star formation occurred in the galaxy disk, and *not* in its nuclear region. The color composites of Fig. 5 and Fig. 12 show that the extinction-corrected FUV and NUV images are clearly tracing stellar populations that appear bluer than other regions. The images in U, B, and R (Figs. 16 and 17) show the transition of the dominant emission from young stellar populations in the SF-regions to older stellar populations in the bulge and center of the galaxy (Fig. 5a). While the extinction corrected image in U is still sensitive mostly to young stellar populations, the R-band image shows that the older stellar populations in the small bulge of NGC 959 become the dominant light source at redder wavelengths, as expected.

Among the FUV–R filters, the largest morphological change as a result of the dust-extinction correction occurs in the optical images, especially in the B-band image. In the FUV, NUV, and U, the light from the younger stellar populations dominates even without applying our dust-extinction correction. Correcting for dust extinction therefore strengthens already discernable galactic

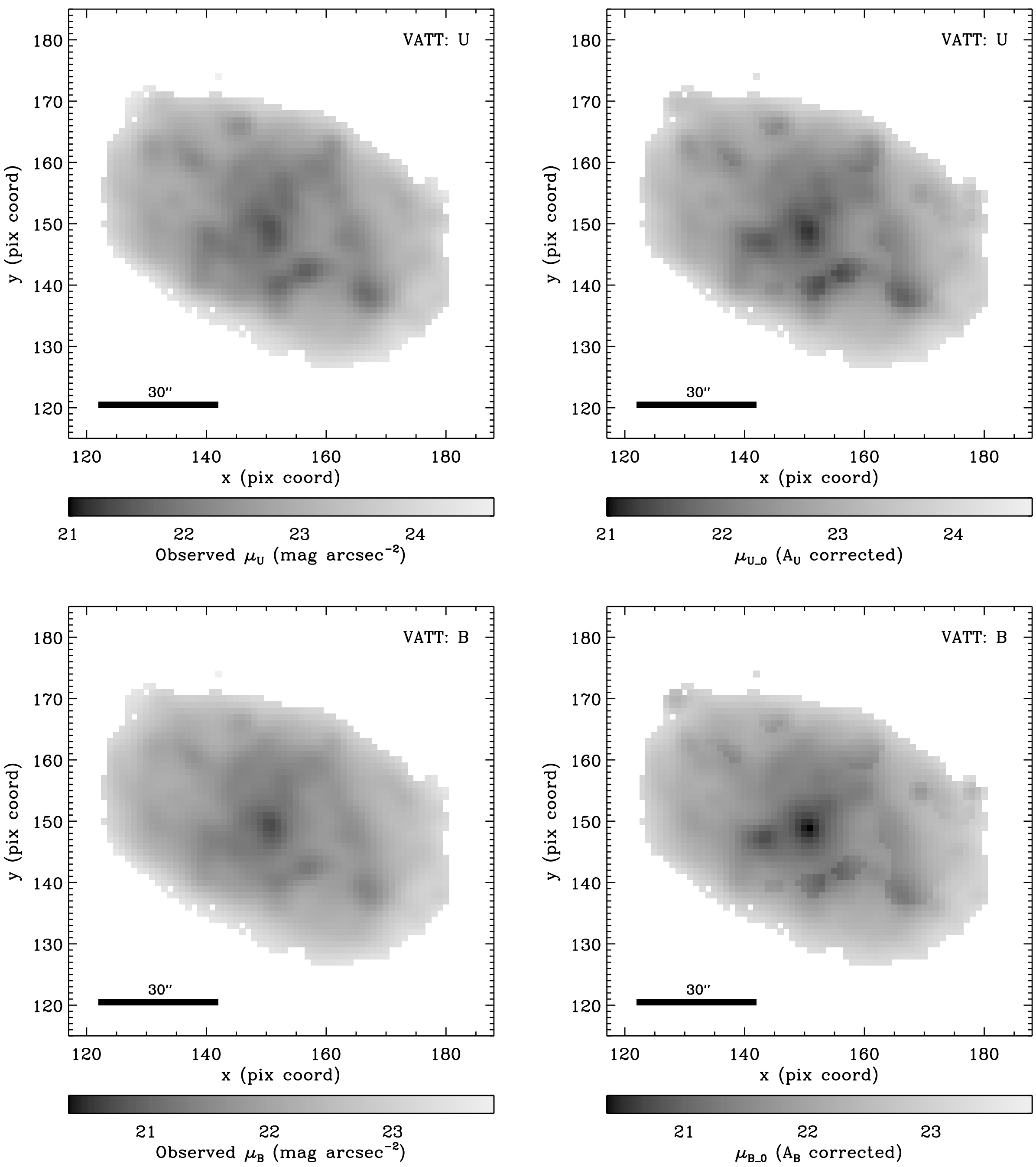

FIG. 16.— Comparison of observed (*left*) and extinction-corrected (*right*) images in the VATT *U* (*top*) and *B* (*bottom*) filters at *GALEX* resolution.

structures, but does not dramatically change the apparent morphology (cf., Windhorst et al. 2002). The *R*-band image, on the other hand, is dominated by light from older stellar populations and suffers to a lesser degree from the effects of dust. The *B*-band samples both younger and older stellar populations (see Fig. 1) and suffers a larger dust extinction than *V* (see Fig. 14 and Table 2). After correction for extinction, light from younger stellar populations that is initially largely hidden behind the dust becomes visible, causing the galaxy morphology to change relatively more in *B* than in other filters.

Previous studies have compared the morphological appearance in *B*- and NIR *H*- or K_s-bands (e.g., Block & Puerari 1999; Elmegreen et al. 1999; Block et al. 2001; Buta & Block 2001; Eskridge et al. 2002; Block et al. 2004; Seigar et al. 2005). Eskridge et al. (2002) compared the morphological classifications in *B* and *H* for ~ 200 spiral galaxies from the Ohio State University (OSU) Bright Spiral Galaxy Survey. They found a relatively good correlation between the classifications in the optical and NIR (see their Fig. 2 and Table 2). On average, the *H*-band classification was found to be ~ 1 T-type earlier than the optical one. Other studies, however,

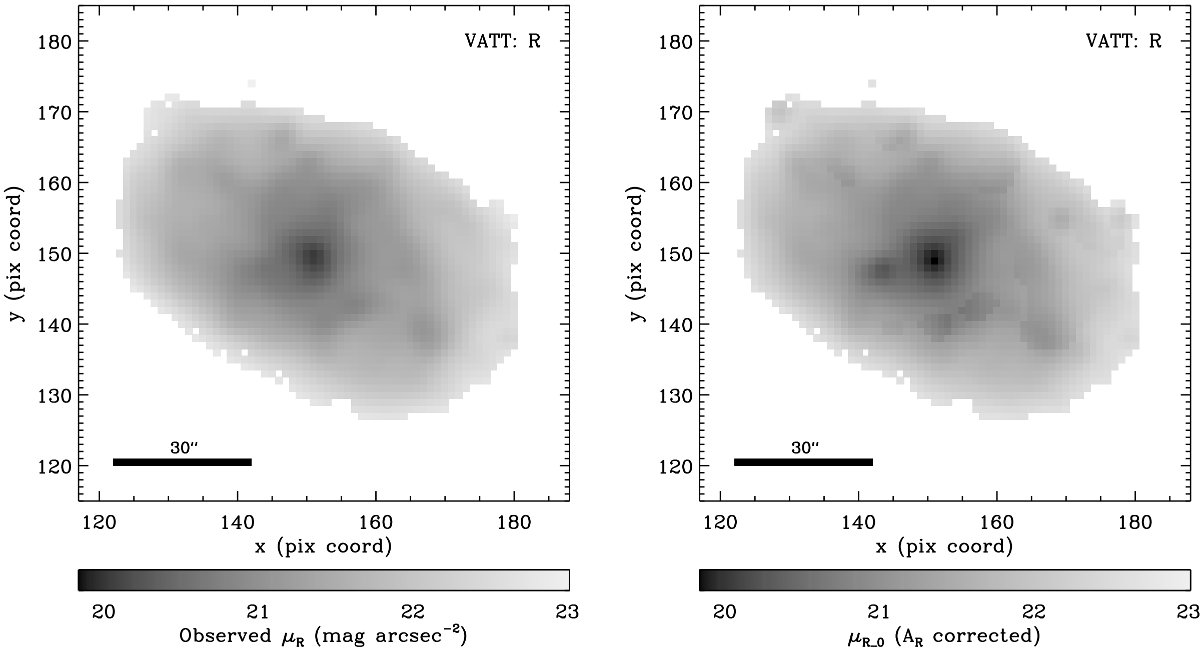

FIG. 17.— Comparison of observed (*left*) and extinction-corrected (*right*) images in the VATT R filter at *GALEX* resolution.

found no correlation between optical Hubble type (Hubble 1926) and dust-penetrated morphological classes for smaller samples of 14–36 galaxies observed in K_s (e.g., Block & Puerari 1999; Elmegreen et al. 1999; Block et al. 2001; Buta & Block 2001; Block et al. 2004; Seigar et al. 2005). Since the Hubble types are based on blue photographic plates, the Hubble classification can be significantly affected by dust extinction (e.g., Windhorst et al. 2002). K_s-band images suffer only 10% of the extinction in V (Fig. 14 and, e.g., Martin & Whittet 1990) and therefore show the stellar distribution with much smaller effects from dust. Therefore, if the amount of dust in (and in front of) a galaxy is significant, the optical B-band is affected accordingly, possibly resulting in drastically different morphology than suggested by the NIR classification. As this was seen in only a small subset of the OSU Bright Spiral Galaxy Survey samples (Eskridge et al. 2002), the galaxy samples used in the K_s-band studies by, e.g., Block & Puerari (1999) may have selected dustier galaxies.

The apparent B-band morphology of NGC 959 before and after extinction correction (bottom panels of Fig. 16) does not differ as drastically as the optical versus K_s morphologies reported in the above studies. But some regions, such as the SE side of the bulge at $[x, y] \simeq [142, 148]$, become much more prominent after extinction correction and the distribution of light becomes similar to that seen at 3.6 and 4.5 μm (see bottom panels of Fig. 13). This means that if a galaxy contains a large amount of dust along major structures, such as a bar or spiral arms, it is possible that the B-band morphology can change significantly after correction for dust.

5. DISCUSSION

Correction for dust extinction is an important, yet challenging issue when studying stellar populations in galaxies, because extinction has a similar effect as stellar population age (e.g., Gordon et al. 1997) and metallicity (e.g., Worthey 1994; Kaviraj et al. 2007b). Failure to correct for extinction will render analyses of stellar populations highly uncertain. Commonly, the FIR/UV flux ratio is used to measure “the” extinction within a galaxy, given as a single averaged extinction value (e.g., Buat & Xu 1996; Calzetti et al. 2000; Boselli et al. 2003; Kong et al. 2004), or as a one-dimensional (i.e., azimuthally averaged) radial extinction profile (e.g., Boissier et al. 2004, 2005). This method assumes that the distribution of dust is relatively uniform across the entire galaxy, or representable by a simple radial extinction gradient. In reality, the distribution of dust is complex, following galactic structures such as SF-regions, bars, and spiral arms. It may also be affected by nearby companions or satellite galaxies. Therefore, a more detailed analysis of the spatial distribution of dust is needed. To obtain a two-dimensional distribution of dust extinction, some studies (e.g., Scoville et al. 2001; Calzetti et al. 2005) use ratios of Hydrogen recombination lines such as Hβ/Hγ, Hα/Hβ, or Hα/Paα, that have known intrinsic values (Osterbrock 1989). This method is applied to measure dust extinction in H II regions within some of the nearest galaxies, but is applicable over only a small fraction of an entire galaxy. Our method, based on the observed V-to-3.6 μm ratio and model SEDs, is able to map the *full* two-dimensional distribution of dust. Fig. 10 and Fig. 11 demonstrate that the actual distribution of extinction within NGC 959 does not follow a simple radial trend and that dust is not concentrated only in the most actively star-forming regions; it is present throughout, tracing the complicated structures from the galaxy center all the way to the outer regions of the disk, where the S/N in the images becomes the limiting factor.

At this point, we would have liked to compare

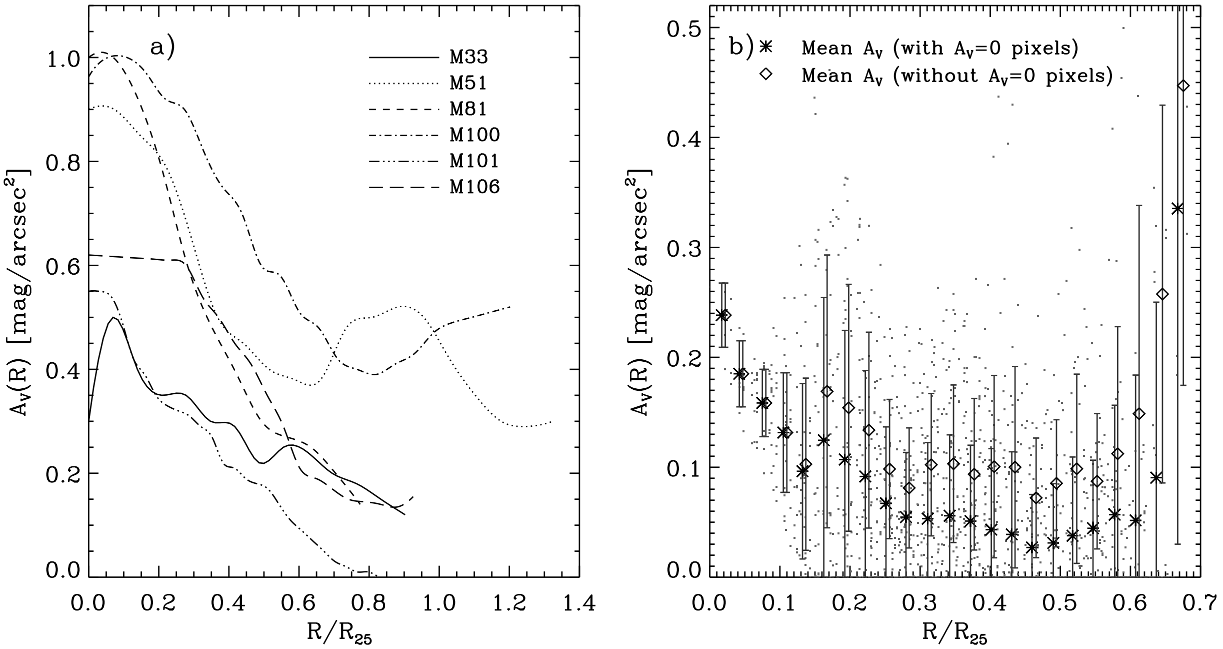

FIG. 18.— *a*) Radial extinction profiles for the six nearby spiral galaxies from Boissier et al. (2004), with distances expressed in units of R_{25}. While some galaxies show a bump or an upturn in the outermost regions of their disk, the extinction generally decreases from the center of a galaxy outward. *b*) Visual extinction, A_V, as a function of distance from the center of NGC 959. Each dot represents the extinction measured in a single pixel. Averages within 0.1 kpc annuli are plotted as asterisks when including pixels with $A_V = 0$ mag arcsec^{-2}, and as open diamonds when excluding such pixels. The error bars represent the standard deviation within each annulus. Twelve pixels with $A_V \gtrsim 0.5$ mag arcsec^{-2} and $R \gtrsim 1.3$ kpc ($R \gtrsim 0.6\,R_{25}$), are not shown here. Note that the very outskirts of NGC 959 may suffer from the light-blending from pixels with S/N $\lesssim 3$ in one or more of the filters, hence rendering the A_V measurements more uncertain.

our results for NGC 959 with extinction measurements from other methods. While Esipov et al. (1991) and Taylor et al. (2005) have studied this galaxy, they did not analyze the internal dust extinction, so we cannot directly compare our results to prior work. However, radial extinction profiles have been analyzed in other galaxies (e.g., Jansen et al. 1994; Boissier et al. 2004, 2005; Calzetti et al. 2005; Holwerda et al. 2009). Jansen et al. (1994) used the special geometry offered by a nearly edge-on disk and a large bulge to demonstrate that the maximum extinction in the dust lanes of two galaxies (UGC 3214 and UGC 3065) decreased outward with distance from the minor axis. Boissier et al. (2004) used the azimuthally averaged FIR/UV flux ratio to measure radial extinction profiles for six nearby late-type spiral galaxies. Their results are reproduced in Fig. 18a, where radius is expressed in units of R_{25}, the major axis radius at the $m_B = 25.0$ mag arcsec^{-2} isophote as listed in the RC3. Each galaxy shows a general trend of decreasing extinction from the center to the outer regions of the galaxy. Boissier et al. (2005) studied the radial profiles of extinction in M 83 using different methods — the Total-IR/FUV luminosity ratio, the UV spectral slope, and the Balmer decrement. Their Fig. 2 of shows that all three methods give similar results: a general decrease of extinction with radius, with a small upturn at the outer edge of M 83's disk. Calzetti et al. (2005) measured the Hα/Paα ratio in H II regions to study the distribution of dust extinction in M 51. Their Fig. 14 shows the distribution of individual extinction measurements as a function of radial distance from the center of M 51. While there are some relatively highly extincted H II regions at outer radii — corresponding to the bump at $R/R_{25} \sim 0.8$ in the profile for M 51 in our Fig. 18a — the distribution does follow the general decreasing trend with increasing radius. On the other hand, Holwerda et al. (2009) used an occulting galaxy pair to measure the distribution and amount of dust via the optical depth against the background galaxy, providing measurements that extend beyond the optically visible disk of the foreground galaxy (see their Fig. 2). They showed that large amounts of dust can exist even in the outermost parts of spiral galaxies, where these dust features are usually undetectable by other means (see their Figs. 11 and 12).

If we see a similar radial trend for our estimated dust extinction in NGC 959 as in the studies above, it would lend additional credence to the reliability of our method. Fig. 18b shows the radial distribution of A_V for each pixel in NGC 959. The galaxy center is located at $[x, y] = [151, 148]$, and the radius is expressed in units of R_{25}. Also indicated are mean extinction values computed within 0.1 kpc bins in radius, with (asterisks) and without (open diamonds) including pixels with $A_V = 0$ mag arcsec^{-2}. The error bars represent standard deviations for the distribution of A_V values in each such bin. While A_V for individual pixels spans a wide range at each radius, the azimuthally averaged extinction, $A_{V,\rm mean}(R)$, clearly decreases from the center outward. At the outermost radial bin, however, the average extinction shoots up to $A_{V,\rm mean}(R) > 0.3$. This is caused mostly by the pixels with high A_V within the "interesting regions" discussed in §3.6.3 (see also Fig. 10), which may or may not be associated with NGC 959. The larger uncertainties for the outermost bins also reflect the fact that these pixels only marginally exceed our minimum S/N criterion in one or more of the filters, hence possibly affecting the reliability of β_V and A_V. Yet, some pixels with relatively high A_V ($0.2 \lesssim A_V \lesssim 0.5$) indicate the existence of dust in the outermost regions of NGC 959, perhaps analogous to the findings of Holwerda et al. (2009). The extensive tests described in previous sections, as well as the general agreement with results from other studies — although they involved different galaxies — give us confidence that our method produces reliable measurements of the spatial distribution of extinction by dust within a galaxy.

An important lesson from the application of our method to NGC 959 is that we are able to map the two-dimensional distribution of dust extinction even from the low-resolution images, which show *no* conspicuous dust features silhouetted against the stars in Fig. 5b. Our initial expectation was that the extinction map created with our method might be relatively featureless, with specific dust features smoothed out. Instead, a map with a complicated pattern that follows the galactic structure emerged (see Fig. 10). A similar, but more detailed dust distribution is recovered when the analysis is repeated on images at the higher IRAC 3.6 μm resolution (Fig. 11). Pixels with large A_V in Figs. 10 and 11 clearly trace the location of silhouetted dust features in the higher resolution VATT (Fig. 5a) or *HST* (Fig. 12) color composites of NGC 959. These results stress that the contrast between regions with high and relatively low extinction can be large within a galaxy disk. At resolutions of $2''\!.2$ (*Spitzer*/IRAC) and $5''\!.3$ (*GALEX*) or ∼110–250 pc at the distance of NGC 959, our method is able to reliably and meaningfully generate a two-dimensional distribution of the dust extinction. Such modest resolutions are accessible and our method will be applicable in galaxies well beyond the Local Group, where the individual dust features may no longer necessarily be spatially resolved.

Our method will also be useful to study dust extinction in galaxies at much larger distances. Once *HST*/WFC3 and *JWST* are in operation, galaxies at $z \simeq 0.3$–0.4 will be easily accessible for such studies, and galaxies at even larger redshifts might be reachable. WFC3[13] has two imaging channels: UVIS covers 0.2–1.0 μm with a pixel-scale of $0''\!.04$ pixel^{-1}, while NIR covers 0.9–1.7 μm at $0''\!.13$ pixel^{-1}. *JWST*[14] will also have two imaging cameras: NIRCam, covering 0.6–5 μm at $0''\!.032$ or $0''\!.065$ pixel^{-1} (Short versus Long Wavelength Channel), and MIRI, which covers 5–27 μm at $\sim 0''\!.11$ pixel^{-1}. At $z \gtrsim 0.3$, the rest-frame V and 3.6 μm bands shift progressively further into the near- to mid-IR regime covered by *HST*/WFC3 and *JWST*, allowing one to apply our method to large numbers of intermediate redshift galaxies. The only limiting factor is the apparent size of the galaxy at these redshifts. Up to $z \simeq 1.6$, the angular scale becomes smaller (Wright 2006) and each pixel samples a larger surface area within a galaxy. At $z \simeq 0.4$, the central wavelengths of the V and 3.6 μm bands shift to 0.77 μm and 5.04 μm, where UVIS and MIRI are expected to deliver resolutions of $0''\!.08$ and $0''\!.195$ FWHM, respectively. This corresponds to ~ 420 pc and ~ 1 kpc, where the latter sets the relevant resolution for our method. While dust lanes will certainly not be visible, we expect our method to still produce meaningful maps of the variations in extinction on scales of ~ 1 kpc, as long as a galaxy is at least several kpc in diameter.

Another application of our method is to investigate the result of Taylor et al. (2005), that the color in the outer regions becomes redder in the majority of late-type spiral and irregular galaxies. This reddening may be caused either by a change in stellar populations or be due to the presence of dust, which is usually only apparent in higher resolution images when silhouetted against a relatively bright stellar background (as in, e.g., Holwerda et al. 2009). In NGC 959, a nearly face-on late-type spiral galaxy, we found evidence for the existence of a moderate amount of extinction in the outermost regions of its disk (Fig. 10). Our method will also be useful to study the dust content of elliptical and lenticular galaxies. In recent years, large amounts of dust were discovered to exist in elliptical and lenticular galaxies, as well as in the halo of spiral galaxies (e.g., Kaviraj et al. 2007a; Oosterloo et al. 2007a,b; Emonts et al. 2008). Since very little SF-activity is ongoing in these galaxies, methods based on the FIR/UV flux ratio or on Hydrogen recombination lines are not as useful as they are for actively star-forming galaxies. Our method, which only depends on images in V and 3.6 μm filters, is well-suited for a study of the distribution of dust within early-type galaxies. We will present a more detailed study of dust distribution in spiral galaxies and in a small number of elliptical and lenticular galaxies — a total of 45 galaxies of all types — in a subsequent paper (Tamura et al. 2009c, in preparation).

A potential future use of our method is to estimate the distribution of dust in simulated galaxy models (e.g., Croton et al. 2006). A detailed two-dimensional analysis of the dust extinction in a large number of galaxies would help understand the properties of dust for different types of galaxies or galactic structures, such as SF-regions, bars, spiral arms, and inter-arm regions. Current simulations are able to model the extinction-free SEDs for many galaxies, while the treatment of internal dust extinction is still broad-stroke. For such models, it will be useful to construct a database of galaxies of different morphological type and mass, to constrain age, metallicity, and the amount and spatial distribution of the dust.

6. CONCLUSIONS

In this paper, we presented a new method for estimating the extinction by dust within galaxies by comparing the observed V-to-3.6 μm flux ratio, β_V, to theoretical SED models. Using a pixel-based analysis, our method is able to estimate the two-dimensional distribution of dust extinction within a galaxy. As a proof of concept, we applied this method to NGC 959, a nearby late-type spiral galaxy. From a pCMD, constructed using an additional U-band image, we robustly selected pixels dominated either by the light from younger stellar populations, or from older ones. Since their intrinsic V-to-3.6 μm flux ratios differ, they were treated separately in our analysis. We presented a two-dimensional map of the visual extinction, A_V, that closely resembles the observed distribution of SF-regions and underlying galactic structures (including a newly identified bar), and which traces the distribution of 8.0 μm PAH emission. Although dust features are inevitably smoothed out to some extent due to light-blending and the low spatial resolution of the images, we were able to construct a two-dimensional extinction map with sufficient detail to delineate the structure of dust features within the disk of NGC 959. We then presented original and extinction-corrected views of NGC 959 from the FUV through MIR. Through a series of tests, we demonstrated the validity of our results and method.

---

[13] Space Telescope Science Institute (STScI), Wide Field Camera 3:
`http://www.stsci.edu/hst/wfc3`

[14] NASA, The *James Web Space Telescope*:
`http://www.jwst.nasa.gov`

Our method has several advantages over other methods based on, e.g., the FIR/UV flux ratio, UV spectral slope, or Hydrogen recombination line ratios. At its core, our method only depends on images in two relatively common broadband filters, V and 3.6 μm (L-band), and is therefore applicable continuously across the face of a galaxy. We exploit the fact that the wavelength-dependent extinction by interstellar dust reaches a minimum near 3.6 μm while it increases toward shorter wavelengths. In V-band, we are sensitive to dust extinction, but fairly insensitive to age and metallicity effects compared to UV–blue filters. We demonstrated that the intrinsic V-to-3.6 μm flux ratio, $\beta_{V,0}$, is well-behaved over a wide range in stellar age and metallicity. While $\beta_{V,0}$ depends on age more strongly than on metallicity, this ratio stays relatively constant for older ($t \gtrsim 500$ Myr) stellar populations, and occupies a relatively narrow range for younger stellar populations. As a result, we can simply compare the observed and intrinsic V-to-3.6 μm flux ratios (after taking mixing or superposition of stellar populations into account) to estimate the amount of dust extinction, A_V, in each pixel. To translate A_V to bluer filters, knowledge of the metallicity become more important (or, alternatively, the uncertainty increases) due to the metallicity-dependence of the extinction curve. This simplicity allows our method — which is mostly automated with only a few manual parameter-settings for each galaxy — to be applied to a large number of galaxies in a very short time.

Since our method does not require visual confirmation or identification of individual dust features, it is applicable to any galaxy beyond the Local Groups, if rest-frame V and 3.6 μm images are available with at least several resolution elements across that galaxy. This offers the possibility of applying our method to *HST*/ACS, *HST*/WFC3, and *JWST* NIRCam and MIRI images to study the two-dimensional distribution of dust not only in the local universe, but also for higher redshift galaxies.

This work was funded by NASA/ADP grant NNX07AH50G. R.A.W. was supported in part by NASA/JWST grant NAG 5-12460. We thank V.A.Taylor-Mager for providing the data observed at the Vatican Advanced Technology Telescope (VATT): the Alice P. Lennon Telescope and the Thomas J. Bannan Astrophysics Facility. We thank the referee for a careful reading and constructive comments that helped improve the paper significantly. We also thank Daniela Calzetti, Seth Cohen, Paul Eskridge, Nimish Hathi, and Russell Ryan for their help, comments, and discussion. This study has made use of the NASA/IPAC Extragalactic Database (NED), which is operated by the Jet Propulsion Laboratory, California Institute of Technology, under contract with NASA, and has used NASA's Astrophysics Data System (ADS) bibliographic services. Additional observations made with the NASA/ESA *Hubble Space Telescope* were obtained from the data archive at STScI, which is operated by AURA, Inc., under NASA contract NAS 5-26555.

REFERENCES

Abraham, R. G., Ellis, R. S., Fabian, A. C., Tanvir, N. R., & Glazebrook, K. 1999, NMRAS, 303, 641
Anders, P., & Fritze-von Alvensleben, U. 2003, A&A, 401, 1063
Bachiller, R. C., & Cernicharo, J. 1986, A&A, 166, 283
Barmby, P., et al. 2006, ApJ, 650, L45
Bell, E. F., Gordon, K. D., Kennicutt, R., C., & Zaritsky, D. 2002a, ApJ, 565, 994
Bell, E. F. 2002b, ApJ, 577, 150
Bertelli, G., Bressan, A., Chiosi, C., Fagotto, F., & Nasi, E. 1994, A&AS, 106, 275
Block, D. L., & Purari, I. 1999, A&A, 342, 627
Block, D. L., Puerari, I., Takamiya, M., Abraham, R., Stockton, A., Robson, I., & Holland, W. 2001, A&A, 371, 393
Block, D. L., Buta, R., Knapen, J. H., Elmegreen, D. M., Elmegreen, B. G., & Puerari, I. 2004, AJ, 128, 183
Boissier, S., Boselli, A., Buat, V., Donas, J., Milliard, B. 2004, A&A, 424, 465
Boissier, S., et al. 2005, ApJ, 619, L83
Boissier, S., et al. 2007, ApJS, 173, 524
Boselli, A., Gavazzi, G., & Sanvito, G. 2003, A&A, 402, 37
Bothun, G. D. 1986, AJ, 91, 507
Brown, R. L., Wild, W., & Cunningham, C. 2004, AdSpR, 34, 555
Bruzual, G., & Charlot, S. 2003, MNRAS, 344, 1000
Buat, V., & Xu, C. 1996, A&A, 306, 61
Buat. V., et al. 2005, ApJ, 619, L51
Buta, R., & Bock, D. L. 2001, ApJ, 550, 243
Byun, Y.-I. 1992, Ph.D. thesis, Australian National University
Calzetti, D., Kinney, A., L., & Storchi-Bergmann, T. 1994, ApJ, 429, 582
Calzetti, D., Armus, L., Bohlin, R. C., Kinney, A. L., Koornneef, J., & Storchi-Bergmann, T. 2000, ApJ, 533, 682
Calzetti, D., et al. 2005, ApJ, 633, 871
Calzetti, D., et al. 2007, ApJ, 666, 870
Caplan, J., & Deharveng, L. 1985, A&AS, 62, 63
Caplan, J., & Deharveng, L. 1986, A&A, 155, 297
Cardelli, J. A., Clayton, G. C., & Mathis, J. 1989, ApJ, 345, 245
Charlot, S., & Fall, S. M. 2000, ApJ, 539, 718
Cohen, M., Wheaton, W., A., & Megeath, S., T. 2003, AJ, 126, 1090
Croton, D. J., et al. 2006, MNRAS, 365, 11
Dale, D. A., Helou, G., Contursi, A. et al. 2001, ApJ, 549, 215
Deo, R. P., Crenshaw, D. M., & Kraemer, S. B. 2006, AJ, 132, 321
de Vaucouleurs, G., de Vaucouleurs, A., Corwin, H. G., Buta, R. J., Paturel, G., & Fouque, P. 1991, Third Reference Catalogue of Bright Galaxies (Springer, New York)
Dickman, R. L. 1978, ApJS, 37, 407
Driver, S. P., Popescu, C. C., Tuffs, R. J., Graham, A. W., Liske, J., & Baldry, I. 2008, ApJ, 678, 101
Elmegreen, D. M. 1980, ApJS, 43, 37
Elmegreen, D. M., Chromey, F. R., Bissell, B. A., & Corrado, K. 1999, AJ, 118, 2618
Elvius, A. 1956, StoAn, 18, 9
Emonts, B. H. C., Morganti, R., Oosterloo, T. A., Holt, J., Tadhunter, C. N., van der Hulst, J. M., Ojha, R., & Sadler, E. M. 2008, MNRAS, 387, 197
Encrenaz, P. J., Falgarone, E., & Lucas, R. 1975, A&A, 44, 73
Eskridge, P. B., et al. 2002, ApJS, 143, 73
Eskridge, P. B., et al. 2003, ApJ, 586, 923

Esipov, V. F., Kyazumov, G. A., & Dzhafarov, A. R. 1991, SvA, 35, 452
Fazio, G. G., et al. 2004, ApJS, 154, 10
Fitzpatrick, E., L. 1999, PASP, 111, 63
Frerking, M. A., Langer, W., D., & Wilson, R. W. 1982, ApJ, 262, 590
Gordon, K. D., Calzetti, D., & Witt, A., N. 1997, ApJ, 487, 625
Gordon, K. D., Clayton, G. C., Misselt, K. A., Landolt, A. U., & Wolff, M. J. 2003, ApJ, 594, 279
Harjunpää, P., & Mattila, K. 1996, A&A, 305, 920
Harjunpää, P., Lethinen, K., & Haikala, L. K. 2004, A&A, 421, 1087
Hayakawa, T., Mizuno, A., Onishi, T., Hara, A., Yamaguchi, R., & Fukui, Y. 1999, PASJ, 51, 919
Hayakawa, T., Cambrésy, L., Onishi, T., Mizuno, A., & Fukui, Y. 2001, PASJ, 53, 1109
Helou, G., et al. 2004, ApJS, 154, 253
Héraudeau, P., & Simien, F. 1996, A&AS, 118, 111
Holwerda, B. W., Keel, W. C., Williams, B., Dalcanton, J. J., & de Jong, R. S. 2009, AJ, 137, 3000
Howarth, I. D. 1983, MNRAS, 203, 301
Hubble, E. P. 1926, ApJ, 64, 321
Jansen, R. A., Knapen, J. H., Beckman, J. E., Peletier, R. F., & Hes, R. 1994, MNRAS 270, 373
Kaviraj, S., et al. 2007a, ApJS, 173, 619
Kaviraj, S., Rey, S.-C., Rich, R. M., Yoon, S.-J., & Yi, S K. 2007b, MNRAS, 381, L74
Kennicutt, R. C., et al. 2003, PASP, 115, 928
Knapen, J. H., Hes, R., Beckman, J. E., & Peletier, R. F. 1991, A&A, 241, 42
Komugi, S., Sofue, Y., Nakanishi, H., Onodera, S., & Egusa, F. 2005, PASJ, 57, 733
Kong, X., Charlot, S., Brinchmann, C., & Fall, S. M. 2004, MNRAS, 349, 769
Koornneef, J., & Code, A. D. 1981, ApJ, 247, 860
Kroupa, P. 2002, Science, 295, 82
Lanyon-Foster, M. M., Conselice, C. J., & Merrifield, M. R. 2007, MNRAS, 380, 571
Leger, A., & Puget, J. L. 1984, A&A, 137, L5
Lejeune, T., Cuisinier, F., & Buser, R. 1997, A&AS, 125, 229
Lejeune, T., & Schaerer D. 2001, A&A, 366, 538
Lindblad, B. 1941, StoAn, 13, 8
Maíz-Apellániz, J., Pérez, E., & Mas-Hesse, J. M. 2004, AJ, 128, 1196
Maraston, C. 2005, MNRAS, 362, 799
Martin, P. G., & Whittet, D. G. B. 1990, ApJ, 357, 113
Mathis, J. S., Rumpl, W., & Nordsieck, K. H. 1977, ApJ, 217, 425
Meurer, G. R., Heckman, T. M., & Calzetti, D. 1999, ApJ, 521, 64
Morrissey, P., et al. 2005, ApJ, 619, L7
Mould, J. R., et al. 2000, ApJ, 529, 786
Nitschelm, C. 1988, A&AS, 74, 67
Oke, J. B. 1974, ApJS, 27, 21
Oke, J. B., & Gunn, J. E. 1983, ApJ, 266, 713
Oosterloo, T. A., Morganti, R., Sadler, E., M., van der Hulst, T., & Serra, P. 2007a, A&A, 465, 787
Oosterloo, T., Fraternali, F., & Sancisi, R. 2007b, AJ, 134, 1019
Osterbrock, D. E. 1989, Astrophysics of Gaseous Nebulae and Active Galactic Nuclei (Mill Valley; University Science Books)
Panuzzo, P., Bressan, A., Granato, G. L., Silva, L., & Danese, L. 2003, A&A, 409, 99
Petersen, L., & Gammelgaard, P. 1997, A&A, 323, 697
Price, S. D., Carey, S. J., & Egan, M. P. 2002, AdSpR, 30, 2027
Regan, M. W., & Mulchaey, J. S. 1999, AJ, 117, 2676
Regan, M. W. 2000, ApJ, 541, 142
Regan, M. W., et al. 2004, ApJS, 154, 204
Relaño, M., Lisenfeld, U., Vilchez, J. M., & Battaner, E. 2006, A&A, 452, 413
Rieke, G. H., et al. 2004, ApJS, 154, 25
Roussel, H., Gil de Paz, A., Seibert, M., Helou, G., Madore, B. F., & Martin, C. 2005, ApJ, 632, 227
Salpeter, E. E. 1955, ApJ, 121, 161
Scalo, J. M. 1986, Fundam. Cosm. Phys., 11, 1
Scoville, N. Z., Polletta, M., Ewald, S., Stolovy, S. R., Thompson, R., & Rieke, M. 2001, AJ, 122, 3017
Seaton, M. J. 1979, MNRAS, 187, 73
Seiger, M. S., Block, D. L., Puerari, I., Chorney, N. E., & James, P. A. 2005, MNRAS, 359, 1065
Sirianni, M., et al. 2005, PASP, 117, 1049
Taylor, V. A., Jansen, R. A., Windhorst, R. A., Odewahn, S. C., & Hibbard, J., E. 2005, ApJ, 630, 784
Trauger, J. T., et al. 1994, ApJ, 435, L3
Trumpler, R. J. 1930, PASP, 42, 214
van Houten, C. J. 1961, Bull. Astron. Inst. Neth., 16, 1
Viallefond, F., Goss, W. M., & Allen R. J. 1982, A&A, 115, 373
Waller, W. H., Gurwell, M., & Tamura, M. 1992, AJ, 104, 63
Walterbos, R. A. M., & Kennicutt, R. C. 1988, A&A, 198, 61
Welikala, N., Connolly, A. J., Hopkins, A. M., Scranton, R., & Conti, A. 2008, ApJ, 677, 970
Whittet, D. C. B., Gerakines, P. A., Hough, J. H., & Shenoy, S. S. 2001, ApJ, 547, 872
Whittet, D. C. B., Shenoy, S. S., Clayton, G. C., & Gordon, K. D. 2004, ApJ, 602, 291
Willner, S. P., et al. 2004, ApJS, 154, 222
Windhorst, R. A., et al. 2002, ApJS, 143, 113
Witt, A. N., Thronson, H. A., & Capuano, J. M. 1992, ApJ, 393, 611
Witt, A. N., & Gordon, K. D. 2000, ApJ, 528, 799
Worthey, G. 1994, ApJS, 95, 107
Wright, E. L. 2006, PASP, 118, 1711
Xu, C., & Helou, G. 1996, ApJ, 456, 152